INVESTIGATION OF EFFECTIVE MEDIUM ABSORBERS FOR POSSIBLE SENSING APPLICATIONS IN THE SUB-1 THZ REGION

A THESIS SUBMITTED TO
THE GRADUATE SCHOOL OF NATURAL AND APPLIED SCIENCES
OF
MIDDLE EAST TECHNICAL UNIVERSITY

BY

OYTUN DEMİRÖRS

IN PARTIAL FULFILLMENT OF THE REQUIREMENTS
FOR
THE DEGREE OF MASTER OF SCIENCE
IN
CHEMISTRY

SEPTEMBER 2022

Approval of the thesis:

INVESTIGATION OF EFFECTIVE MEDIUM ABSORBERS FOR POSSIBLE SENSING APPLICATIONS IN THE SUB-1 THZ REGION

submitted by **OYTUN DEMİRÖRS** in partial fulfillment of the requirements for the degree of **Master of Science** in **Chemistry, Middle East Technical University** by,

Prof. Dr. Halil Kalıpçılar
Dean, Graduate School of Natural and Applied Sciences _______________

Prof. Dr. Özdemir Doğan
Head of the Department, Chemistry _______________

Prof. Dr. Okan Esentürk
Supervisor, Chemistry, METU _______________

Examining Committee Members:

Prof. Dr. Hakan Altan
Physics, METU _______________

Prof. Dr. Okan Esentürk
Chemistry, METU _______________

Assoc. Prof. Dinçer Gökcen
Electrical and Electronics Engineering, Hacettepe University _______________

Assoc. Prof. Halil Berberoğlu
Physics, Ankara Haci Bayram Veli University _______________

Asst. Prof. Demet Asil Alptekin
Chemistry, METU _______________

Date: 02.09.2022

I hereby declare that all information in this document has been obtained and presented in accordance with academic rules and ethical conduct. I also declare that, as required by these rules and conduct, I have fully cited and referenced all material and results that are not original to this work.

Name Last name : Oytun Demirörs

Signature :

ABSTRACT

INVESTIGATION OF EFFECTIVE MEDIUM ABSORBERS FOR POSSIBLE SENSING APPLICATIONS IN THE SUB-1 THZ REGION

Demirörs, Oytun
Master of Science, Chemistry
Supervisor : Prof. Dr. Okan Esentürk

September 2022, 73 pages

Imaging in the terahertz (THz) region has receiving great attention in recent years with its very attractive diverse application possibilities from security to health, from bio to material inspection. However, the nature of the THz frequency region brings many challenges to development of sources and sensors for imaging applications. Some of the challenges are requirement of large pixel-pitches, high fabrication and maintenance costs, and low emission levels of the sources at room temperature. Due to the strong atmospheric attenuation of THz waves above 1 THz, it is better to produce a sensing pixel operating in frequencies below 1 THz. Large pixel pitches for long wavelengths and thicker absorber layers due to the low absorption coefficients that result in higher thermal mass causes challenges in microfabrication and, thus, in sensing applications. Because of these limitations, a unique absorber design for the THz region is required to get lighter antenna structures for THz sensors. In this study, with an aim of tuning THz response of absorber and antenna structures, TiAlV periodic elements with various sizes embedded into Si_xN_y films were designed, prepared on p-type silicon substrate, and evaluated using THz time-

domain spectroscopy. The designs were supported *in silico* with Bruggeman Effective Medium Theory simulations. The experimental properties were found to be in agreement with the simulations in part. The deviation is possibly due to the limitation in the making of the model structure and also possibly due to the simplification of the model relative to the experimental structure. Overall, effects of fabrication parameters on the THz response of the thin films are compared and reported. Further optimization of the process flow for appropriate wafer level uniformity is needed for the thin films with higher (around 30%, volumetric) metal content.

Keywords: Terahertz**,** Absorber, Thin film, Effective medium, Absorption

ÖZ

1 THZ ALTI BÖLGEDE OLASI ALGILAMA UYGULAMALARI İÇİN ETKİN ORTAM SOĞURUCULARIN İNCELENMESİ

Demirörs, Oytun
Yüksek Lisans, Kimya
Tez Yöneticisi: Prof. Dr. Okan Esentürk

Eylül 2022, 73 sayfa

Terahertz (THz) bölgesinde görüntüleme, güvenlikten sağlığa, canlı dokudan malzeme denetimine kadar çok çekici çeşitli uygulama olanakları ile son yıllarda büyük ilgi görmektedir. Bununla birlikte, THz frekans bölgesinin doğası, görüntüleme uygulamaları için kaynak ve sensörlerin geliştirilmesine birçok zorluk getirir. Zorluklardan bazıları, mevcut yüksek üretim ve bakım maliyetinin yanı sıra geniş piksel aralıkları gereksinimi ve kaynakların oda sıcaklığında düşük emisyon seviyeleridir. 1 THz'in üzerindeki THz dalgaların atmosferde yüksek kaybı nedeniyle, 1 THz'in altındaki frekanslarda çalışan bir algılama pikseli üretmek daha iyidir. Uzun dalga boyları için büyük piksel aralıkları ve daha yüksek termal kütle ile sonuçlanan düşük absorpsiyon katsayıları nedeniyle daha kalın emici katmanlar, mikrofabrikasyonda ve dolayısıyla algılama uygulamalarında zorluklara neden olur. Bu sınırlamalar nedeniyle, THz sensörleri için daha hafif anten yapıları elde etmek için THz bölgesi için benzersiz bir soğurucu tasarımı gereklidir. Bu çalışmada, THz soğurucu ve anten yapılarının THz tepkisini ayarlamak amacıyla, SixNy filmlere gömülü çeşitli boyutlarda TiAlV periyodik elemanlar tasarlanmış, p-tipi silikon altlık üzerinde hazırlanmış ve THz zaman alan spektroskopisi kullanılarak

değerlendirilmiştir. Tasarımlar Bruggeman Etkili Ortam Teorisi simülasyonları ile *in silico* olarak desteklenmiştir. Deneysel özelliklerin simülasyonlarla uyumlu olduğu bulunmuştur. Ölçüm ve simülasyon arasındaki sapma, muhtemelen model yapısının yapımındaki sınırlamadan ve modelin deneysel yapıya göre basitleştirilmesinden kaynaklanmaktadır. Sonuç olarak, fabrikasyon parametrelerinin ince filmlerin THz tepkisi üzerindeki etkileri karşılaştırılmış ve rapor edilmiştir. Daha yüksek (yaklaşık %30, hacimsel) metal içeriğine sahip ince filmlerin üretimi için proses akışının daha fazla optimizasyonu gereklidir.

Anahtar Kelimeler: Terahertz, Soğurucu, İnce film, Etkin ortam, Soğurulma

To all stray cats

ACKNOWLEDGMENTS

First and foremost, I would like to express my gratitude to my supervisor Prof. Dr. Okan Esentürk and Prof. Dr. Hakan Altan for their guidance, and for numerous opportunities they provided.

I would like to express my sincerest gratitude to Emrah Dirican, Bahar Atik and all researchers at METU MEMS Center for teaching all things I know about cleanroom environment and processes.

I would like to thank each and every member of LSG for their help and support.

Also I would like to thank the jury members Asst. Prof. Demet Asil Alptekin, Assoc. Prof. Halil Berberoğlu, and Assoc. Prof. Dinçer Gökcen for their interest in this study.

Finally, my lovely wife Berna, my wonderful parents İnci, Murat, Bahar and Sinan, my sisters Olgu and Derya: I would like to thank you for your endless support.

Last but not least, I would like to thank *my framily:* Doruk, Ege, Ezgi, Görkem, Kutay, Selena, Serkan, and Tarkan.

TABLE OF CONTENTS

ABSTRACT v

ÖZ vii

ACKNOWLEDGMENTS x

TABLE OF CONTENTS xi

LIST OF TABLES xiii

LIST OF FIGURES xiv

INTRODUCTION 1

1.1 Terahertz (THz) Region 2

1.2 Microbolometer Technology 3

1.2.1 Working Principle of Uncooled Microbolometers 4

1.3 Terahertz Time Domain Spectroscopy 7

1.3.1 Terahertz Generation 7

1.3.2 Terahertz Detection 11

1.4 Effective Media and Thin Films 12

1.4.1 Bruggeman Effective Medium Theory 12

2 .... MATERIALS AND METHODS 15

2.1 Fabrication Methods 15

2.1.1 Magnetron Sputtering 15

2.1.2 Photolithography 17

2.2 Fabrication of Effective Medium Thin Films 26

2.3 Terahertz Characterization 29

2.4 Terahertz Time Domain Spectrometer 29

3..RESULTS & DISCUSSION 33

3.1 Preliminary Works 33

3.1.1 Optimization of the Thickness of Dielectric Layer 33

3.1.2 Optimization of the Thickness of the Metal Layer 34

3.1.3 Optimization of the TiAlV Etch Process 35

3.2 SEM-EDX Characterization 38

3.3 Influence of the etching time on the THz response 43

3.4 Influence of the Volumetric Metal Content 51

3.5 Effect of Annealing on the THz Transmission 58

3.6 Calculated Refractive Index of the P-Type Silicon 59

3.7 Simulated vs Measured Data 62

4...CONCLUSION 65

REFERENCES 67

LIST OF TABLES

TABLES

Table 1 - Thickness values of Patterned TiAlV layer on the numbered areas of an 8" Wafer 35

Table 2 - Elemental ratios in the thin film coated with the element ratios in the target material 39

Table 3 - Elemental analysis of the SQ1 sample with SEM-EDS 41

Table 4 - Thickness vs sheet resistance values of TiAlV thin-films....................... 44

LIST OF FIGURES

FIGURES

Figure 1 - THz region in the electromagnetic spectrum 3
Figure 2 - Representative perspective view of a microbolometer pixel [19] 4
Figure 3 - Atmospheric Attenuation of the THz Signals[27] 6
Figure 4 - Structural Diagram of the PCA[29] 7
Figure 5 - THz Generation Process (a) in the physical form, red beam is the optical and the green one is the generated THz beam (b) on the energy diagram of energy bands of the semiconductor with optical illumination and electrical bias[32] 9
Figure 6 - The diagram of THz detection configuration in our setup for electro-optical sampling[34] 11
Figure 7 - Schematic diagram of the sputtering chamber 16
Figure 8 - Adhesion Promotion for Silicon Wafer 19
Figure 9-Diazonaphtoquinine - Sulphonate 20
Figure 10 - Novolak 21
Figure 11 – Solubility diagram of the photolithographic process[54] 22
Figure 12 - Transferring a pattern on the metal layer with a positive tone photoresist 23
Figure 15 – Schematic fabrication steps of the patterned thin-film structures (Top and Cross-sectional view) 26
Figure 14 - Unit cells of the patterned thin-films 28
Figure 17 - Schematic Diagram and the Photo of the home-made THz-TDS Setup[9] 30
Figure 18 - FFT parameters that used in the Origin Pro Software 31
Figure 17 - Numeric Labels of the measured areas of the 8" Wafer 34
Figure 18 - Over-etched thin film with die number #24 in a) naked eye and b) 150x optical zoom 36
Figure 19 - Optical microscope images of a) SQ1-10s 37

Figure 20 - a) Cross-sectional SEM of the TiAlV layer b) EDX analysis spectrum of the TiAlV 38
Figure 21 Elemental percentages of the inspected surface 39
Figure 22 - SEM Image of SQ2 Sample with 30000x magnification 40
Figure 23 - Elemental map of the EDS Results 42
Figure 24 - Cross-sectional diagram of the fabricated thin-films 43
Figure 27 - Optical Microscope images of the patterned thin-films with 150x magnification 45
Figure 26 - Peak amplitudes of the THz profile in time domain of SQ2 samples etched for 10, 15, and 20 seconds 46
Figure 27 - THz time domain data of the samples with the 10-second dipping to the etchant solution 47
Figure 28 – Magnified version of the Figure 27 to its peak region 48
Figure 29 - THz time domain data of the samples with the 15-second dipping to the etchant solution 49
Figure 30 - Magnified version of the Figure 28 to its peak region 49
Figure 31 - THz time domain data of the samples with the 20-second dipping to the etchant solution 50
Figure 32 - Magnified version of the Figure 30 to its peak region 50
Figure 33 - THz response of the PR protected, non-patterned parts of the wafers after 10,15, and 20 seconds of dipping to the etchant solution 51
Figure 34 - Schematic fabrication steps of the patterned thin-film structures with higher volumetric metal content (Top and Cross-sectional view) 52
Figure 35 - SEM-EDS Analysis After Plasma Etching, Elemental Ti Analysis Confirmed Etching Complete 54
Figure 36 - Images of 150x magnified thin films with higher metal content 54
Figure 37 - Time Domain Data of the thin films 55
Figure 38 - Power Transmission data of the thin-films with higher metal content (with respect to air - through iris-) 56
Figure 39 - Cross sectional measurement of the S1.2 and S1.6 samples 57

Figure 40 - Time Domain Data of the samples before and after annealing 58
Figure 41 - FFT parameters that used in the Origin Pro Software 59
Figure 42 - THz-TDS Spectrum of the P-Type Si with respect to air 60
Figure 43 - Calculated n and k values of P-type Silicon 61
Figure 44 - Frequency Domain Power Transmission Data with respect to Air (SQ1, SQ2, and CIRC)..63
Figure 45 - CST Microwave Simulations of the thin-films (Completed by Prof. Dr. Hakan Altan) 64
Figure 46 - Simulated effective mediums 64

CHAPTER 1

INTRODUCTION

Terahertz (THz) waves has interesting properties such as low ionization energy and high permeability. Due to these properties, THz technology attracting significant attention in areas such as safety applications, real-time industrial quality control, nondestructive testing, and medical applications.[1]–[10] For sensor applications, however, it is essential to develop unique materials to maximize spectral response at THz frequencies in order to take advantage of this region of the electromagnetic spectrum.

Uncooled THz detectors based on microbolometer technology have also attracted attention due to advantages such as cost-effectiveness, room temperature operation and suitability for mass production, as compared to those operating at cryogenic temperatures. Uncooled microbolometer technology has confirmed its success in the infrared region. However, detecting THz waves with an uncooled bolometer has its own appeal. Operating in the sub-1 THz region is more advantageous due to low atmospheric absorption, but this comes with its tradeoffs.

Uncooled infrared detectors based on microbolometer technology, realized with MEMS, are used in many applications. Recently, it has been recognized that imaging in the terahertz band has advantageous sensing applications for security purposes. However, these systems are still not widely used due to their limited sensitivity and high cost. It is possible to overcome these problems with a detector that displays real-time images, such as a microbolometer. However, some limits must be overcome for this. A metal-based thin film with a high absorption capacity in the infrared region cannot be used efficiently due to its high reflection coefficient in the THz region. In terms of many security and medical imaging applications, there is the

need to develop sensor arrays of high sensitivity. THz Sensor arrays have the potential to achieve this necessary high sensitivity since interference of the atmosphere is minimal in this region. However, the existing microbolometer production technologies fail to achieve the necessary pixel dimensions due to proportionally increasing thermal mass. Since the radiation emitted by an object around room temperature in the THz band is much lower than that in the infrared band, it becomes difficult to detect remotely. These considerations highlight that the absorber layer should be designed specifically in the sub-1 THz frequency region.

This study aims to increase the sensitivity of absorption with metal-embedded media thin film systems that will be developed specifically in the THz region. By reducing the thermal mass of the absorber structure, optimizing the dielectric properties of the active medium, and minimizing the THz reflection according to the pixel dimensions, it will be ensured that the response and sensitivity of the microbolometer sensors will be increased with the original metamaterial structures for future studies.

1.1 Terahertz (THz) Region

Terahertz (THz) region of the electromagnetic spectrum lies between microwave and infrared regions (0.1-10 THz). Because of the lack of suitable detector and source technologies, this region is also called "THz gap".[1] THz technologies have been heavily studied in the fields of astronomy and astrophysics[2], and the know-how emerged from these fields have created a foundation for new technologies like high-speed telecommunication technology (6G) [3], molecular spectroscopy[4], security and surveillance systems[5]–[8], and pharmaceutical detection[9]–[12]. However, all those research fields are heavily dependent on suitable sources and detectors for the implementation and development of new THz technologies. Absence of appropriate generation/detection system is still a bottleneck for many promising areas.

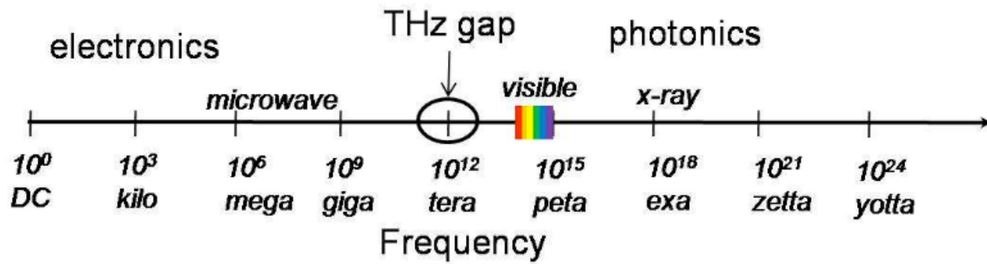

Figure 1 - THz region in the electromagnetic spectrum

It is fundamentally important to develop unique sensing technologies in order to exploit the promising properties of the THz region. Since microbolometer technology has provided successful sensing devices in the infrared (IR) region,[13] uncooled THz detectors based on microbolometer technology have also gathered attention as a probable sensing solution.[14]–[17] However, implementing the microbolometer technology in THz region has its own trade-offs. Despite working in the sub-1 THz region being more favorable due to the lower atmospheric absorption,[18] wavelength in the sub-1 THz region is larger than 300 µm. That means successful detection of the THz waves requires significantly larger pixel size compared to IR microbolometers that operate in the 8-12 µm region. Moreover, many design tricks that are used to increase the absorption level of the incident radiation may not be suitable in the THz region because of the large wavelength. All the design and fabrication limitations will be covered in the next section in detail.

1.2 Microbolometer Technology

The main challenge with developing an uncooled microbolometer pixel for the THz region is performing high absorption without increasing pixel size and the resultant thermal mass of the detector. To achieve that, the pixel material and design is explored for specific absorption frequencies. Developing proper effective mediums for the desired electromagnetic response can be a solution.

1.2.1 Working Principle of Uncooled Microbolometers

In microbolometer structures, the pixel consists of an upper absorber and a lower active material layer. This structure provides a change in resistance with changing temperature. This structure is suspended and isolated using microfabrication techniques, thus providing high thermal insulation from the underlying readout circuit.

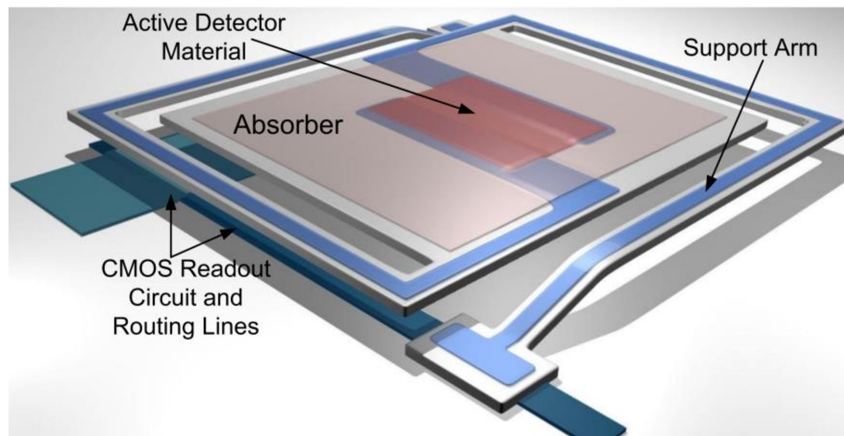

Figure 2 - Representative perspective view of a microbolometer pixel [19]

Incident radiation is absorbed by absorber layer and converted into thermal energy. Absorber layer and the active detector material are in contact with each other; a convective heat transfer occurs between two bodies. The electrical resistivity of the active material layer is heavily dependent on material's temperature. Therefore, temperature change in the structure can be interpreted by readout circuit as resistance and voltage change in the circuit.

Uncooled microbolometer technology has validated its success in the infrared region.[13] Uncooled THz detectors based on microbolometer technology have also gathered attention due to their advantages of cost-effectiveness, ability to operate at room temperature, and feasibility of mass production.[5] However, implementation of the microbolometer technology into THz region comes with some design

challenges. One performance criterion in thermal sensors is the time constant of the sensor. It is a parameter with proportional response time of the sensor. Time constant can be described as:

$$\tau = \frac{C}{G} \qquad \text{(Equation 1)}$$

C Thermal capacitance [J/K]

G - Thermal conductance [W/K]

Another factor affecting the sensitivity of the microbolometer pixel associated with the structure is the thermal mass of the structure. As the thermal mass increases, the response times, defined by the time constant, increase accordingly. Thus, limiting the sensitivity of the pixel. In the light of these factors, many studies focus on the optimization of microbolometers in the infrared region. It is seen that researchers have been working on unique and extraordinary methods in recent years [6], [16], [20]–[26], since the wavelengths in the THz region are much longer, they have less energies. Most importantly, the intensity of the rays coming from the objects radiating at room temperature is much lower, and the size of these structures are in the micron scale.

However, the microbolometer structures produced in the studies generally work in the region above 1 THz. But, in terms of security applications, the region below 1 THz is quite suitable for hidden object detection. Since the scattering decreases as the wavelength increases, the penetration of long wavelengths in insulating media is also higher. For this reason, a frequency range of less than 1 THz is preferred in security applications to identify and detect hidden objects. The THz absorption spectrum of air is dominated by the characteristic peaks of water and oxygen. (see Figure 3).

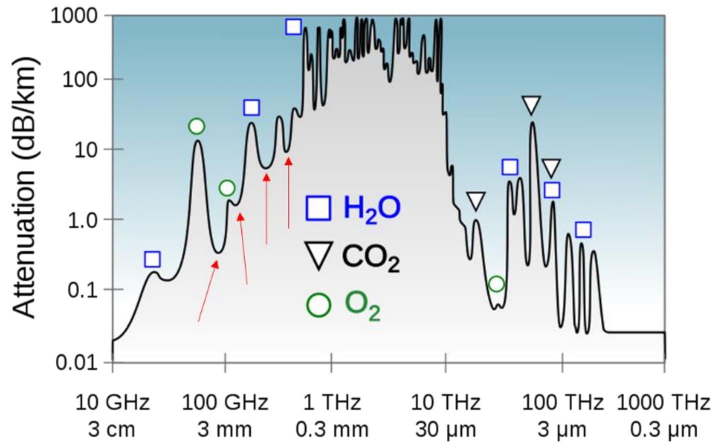

Figure 3 - Atmospheric Attenuation of the THz Signals[27]

In the region where the THz radiation frequency is 1 THz and above, there are many absorption bands close to each other and it is difficult to separate the transmission bands from the absorption bands. In the 0.1 –1.0 THz frequency range, the number of absorption bands is much less and the 0.5 THz, 0.65 THz and 0.87 THz transmission bands are notable as promising windows for imaging applications.[6], [18], [27] In summary, frequencies below 1 THz are less affected by humidity in the air. It would be advantageous to work in the region below 1 THz in order to minimize the losses caused by the air absorbing THz radiation. However, the application of quarter wavelength layer thicknesses, which are generally used to increase absorption in IR microbolometers, at wavelengths sub-1 THz (mm range) is extremely difficult in terms of microfabrication. One of the most important problems is the high reflectivity of the metal-thin films used as the absorber layer in the THz region due to their negative dielectric properties. coefficient they have. In sub-1 THz region this situation is even more problematic. To prevent this, each unit taking part in the absorber layer structure should be adapted to the THz frequency region in an optimized way according to its dielectric properties. Decreased reflection of the incident wave and high dissipation in the medium can be achieved by using tailored thin-film structures with equal impedance to incident medium and a high extinction coefficient.[28] In this study, we investigated an effective medium approach using

metamaterials whose dielectric properties can be tailored to maximize THz absorption.

1.3 Terahertz Time Domain Spectroscopy

1.3.1 Terahertz Generation

The THz wave generation in this study based on a PCA antennas used in the home-made setup. First, short laser pulses with a pulse width of less than 1 picosecond (spa) are focused between the electrical contacts of the PCA. The photons in the laser pulse have a photon energy (E = h.ν) greater than the energy gap of the semiconductor thin-film (E_g) and are absorbed by the film. Each absorbed photon creates a hole for free electrons in the conduction band and creates an electron in the valence band of the material, making it electrically conductive for a short time before the carriers are recombined with each other.

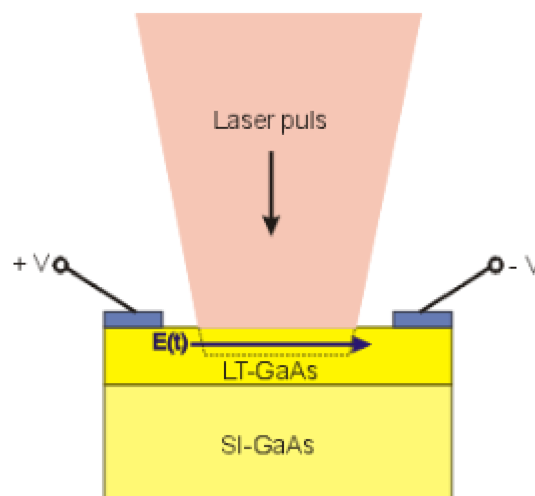

Figure 4 - Structural Diagram of the PCA[29]

A typical photoconductive antenna for THz region consists of a semiconductor thin film and two separated conductive contact pads. In the Figure 4, cross-section of the PCA can be seen. Semiconductor part is III-V compound in most cases such as GaAs.[30] The PCA that used in this study has a highly resistive semi-insulating GaAs substrate (SI-GaAs). Since, SI-GaAs is highly resistive material, its carrier lifetime is relatively long, about 500 ps. However, the upper side of the film which consists of GaAs must much shorter carrier lifetime to produce THz waves. Because 1 THz is equal to $1x10^{12}$ Hz, separated carriers in the film must recombine within a time interval smaller than 1 ps. To create this short carrier time, some crystal defects are created by purpose. For instance, these defects are created with low temperature growth (between 200-400ºC) in the GaAs films and that films will have some arsenic clusters at the end of the low temperature growth. Adding defects to the film is made possible fast radiative recombination of the electron-hole pairs which is under 1 ps. [31]

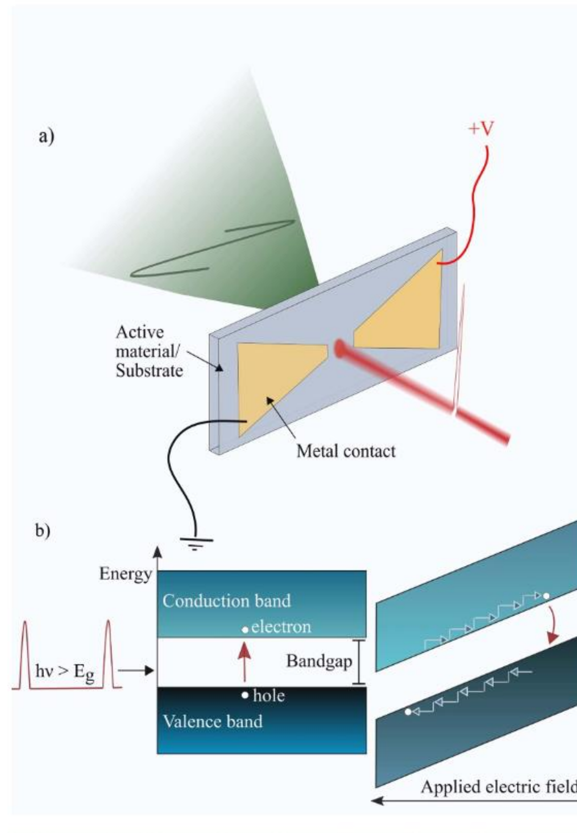

Figure 5 - THz Generation Process (a) in the physical form, red beam is the optical and the green one is the generated THz beam (b) on the energy diagram of energy bands of the semiconductor with optical illumination and electrical bias[32]

The THz generation mechanism can be seen in the Figure 5, while an electrical field applied between electrode pads, an ultrafast optical beam which has greater energy than the bandgap of the semiconductor, is focused between the electrodes. Therefore, resultant free carriers formed during light illumination, and they are accelerated due to applied bias voltage. The acceleration of the carriers and their subsequent recapturing radiates an electromagnetic pulse at THz frequencies. Since the transient current and the resultant THz radiation relies on the accelerating and recapturing carriers, generated radiation is always parallel with the electrical field between metal electrodes. (Figure 5-a) Moreover, the radiated THz waveform ($E_{\mathrm{THZ}}(t)$) can be

expressed as the derivative of the generated photocurrent between the metal electrodes (I_{pe}(t)) (Equation 3). [33]

$$E_{THZ}(t) = \frac{\mu_o \omega_o}{4\pi} \frac{\sin\theta}{r} \frac{d}{dt_r} [I_{pc}(t_r)]\theta \propto \frac{dI_{pc}(t)}{dt} \qquad \text{(Equation 2)}$$

Here, μ_0 is the magnetic permeability of free space, ω_0 is the optical excitation spot size, r is distance from the device from the device, and θ is angle from the device (normal to the surface).

The overall performance of the emitter PCA is heavily influenced by material's optoelectronic properties and the electrode geometry. [33]

1.3.2 Terahertz Detection

In this study, THz detection is performed by electro-optic (EO) sampling in this study. This method relies on electric field modulation of an electro-optic material to birefringence (splitting a ray into two parallel rays that polarized perpendicular to each other) and detection of the split rays with balanced photodiodes. The relationship with change in polarization and electric field of incident THz pulse was formulated in detail by G. Gallot and D. Grischkowsky in 1999 [34]

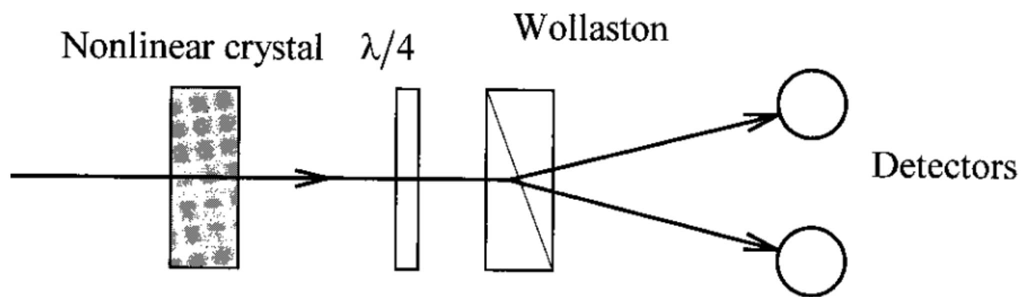

Figure 6 - The diagram of THz detection configuration in our setup for electro-optical sampling[34]

In this study, the beam transmitted inside the sample is focused to a 500 μm thick <110> ZnTe crystal (MTI Corporation) and detected using electro-optic detection method (Figure 6) with a balanced photodiode and lock-in amplifier. The degree of change in polarization and time delay between optical probe beam and the THz pulse can be used to map THz waveform. [35]

1.4 Effective Media and Thin Films

Effective media and thin films are usually electronic artificial materials with composite repetitive structures on an unnatural subwavelength scale. *Via* careful selection of the constituent materials and the structural geometry, metamaterials can be tailored to desired electric and magnetic resonances at specific regions of the electromagnetic spectrum. In nature, atoms of different elements exist in crystal lattices of different geometries. It is known that crystal structures can display macroscopic properties that are different from their constituent elements and provides a massive variety to the material scientists. However, natural materials and their miscellaneous properties are restrained by fundamental rules of physical chemistry. On the other hand, the properties of artificial materials are limited by only our imagination and creativity. Due to this freedom of the design and the possibility for creation of many custom-tailored responses from a material, artificial materials have attracted considerable attention in the recent years. [36]–[49]

1.4.1 Bruggeman Effective Medium Theory

Bruggeman effective medium theory is an approximation of two-phase inhomogeneous materials to determine the effective dielectric permeability of the medium expressed as random unit cells. One of the main differences between Maxwell-Garnett (another famous effective medium approximation) and Bruggeman approximations is the distribution of the phases.

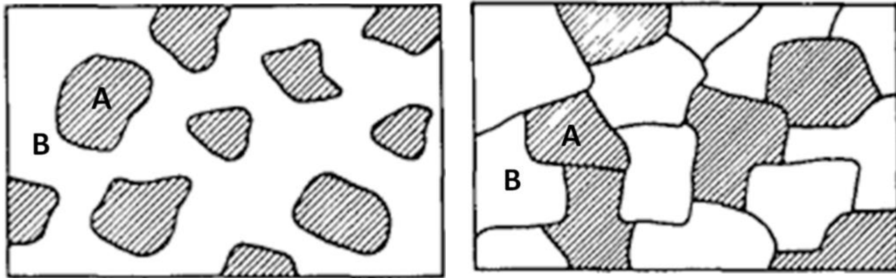

a) Separated-grain microstructure for heterogeneous two-phase media

b) Aggregate microstructure for a heterogenous two-phase media

Separated grain structure is the distribution model which is accepted in Maxwell-Garnett effective medium theory which has components with role as inclusion (phase A) and as host (phase B). (Figure 7-a) On the contrary, in Bruggeman effective medium theory, the components play the same role in the aggregate microstructure model. (Figure 7-b)

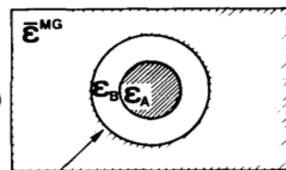

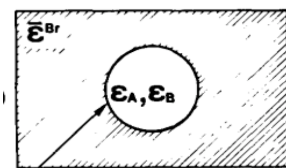

The other fundamental difference of both theories comes from the filling factor "f" interpretation of the unit cells. In Maxwell-Garnett approximation which uses separated-grain structure, a random unit cell is represented as two spheres, one of

them is a core (inclusion material) with permeability ε_A and the host material with permeability ε_B surrounds the inclusion material.

However, the unit structure of Bruggeman's model has the structural equivalence of the two constituents, which means it has a single sphere with permeability ε_A with f probability and ε_A with 1-f probability. Relationship between dielectric permeability of the components and the overall effective medium permeability was reported in 1935 by D.A.G. Bruggeman. By using tailored effective thin-films, a highly efficient absorber structure for sub-1 THz region may be fabricated. This study aims to investigate effect of sub-wavelength sized periodic effective medium films to understand their response to the THz signals for possible sensor applications.

CHAPTER 2

MATERIALS AND METHODS

In this chapter, the fabrication process of the absorber devices described in detail. The proposed effective medium thin films were fabricated by microfabrication steps like lithography, magnetron sputtering. Detailed steps and parameters given in Section 2.2.

2.1 Fabrication Methods

2.1.1 Magnetron Sputtering

Sputter deposition is the one of the physical vapor deposition (PVD) methods for thin-film applications which a solid-state material is ejected from a target material into the gas phase by bombarding them with energetic atoms. The main mechanism of the sputtering is using partially ionized gas (plasma) created in a vacuum environment, on the target material, and ejecting atoms one by one with collisions of the ionized gas particles. The sputtering method can be used to construct thin films a variety of materials such as metals, dielectrics, and semiconductors.[50]

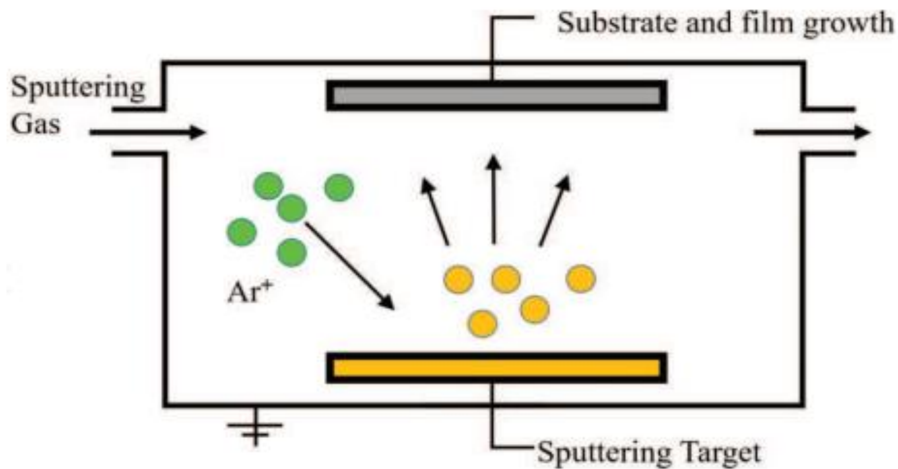

Figure 7 - Schematic diagram of the sputtering chamber

While in the simple cathode sputtering only an electric field applied through cathode (target) and anode (substrate), in the magnetron sputtering there is an additional magnetic field generator located in the cathode. Positive and negative charges not only influenced by electrical fields, and also deflected into the target surface by magnetic field. Charge carriers focused on the center of the target because magnetic end electrical fields become perpendicular at the center of the target. This application increase ion-target collisions on the target material due to increased path of the charge carriers and achieves low operational temperature, low damage, and high speed.

In our fabrication, a thickness of 30 nm TiAlV layer (90/6/4 %wt) deposited on Si_xN_y layer with AJA confocal sputtering systems. The sputtering target has dimensions of 100 cm diameter and 6.35 mm in thickness. The chamber pressure was 3 mTorr and Argon flow was 30 sscm. The deposition rate of the system was 7.2 nm/min that measured with Veeco Dektak Surface Profiler (250 seconds of coating time results with 30.5 nm thin film thickness).

2.1.2 Photolithography

One of the major improvements in lithography technique has accidentally performed by a playwright named Alois Senefelder in 1798. He was found that when he immersed limestone plates in the nitric acid, wax letters written on the plate transferred into the limestone. The wax covered regions were unaffected by the nitric acid while uncovered limestone was etched, making possible transfer for any wax pattern to the stone. This discovery used by him to create templates for duplicating patterns by limestone. By drawing and writing on the limestone plate with an oily ink and introducing it an acidic solution, he could create topographical printing templates. When an ink roller introduced across the surface of the limestone, only the areas protected with oily ink, covered with printing ink. After printing ink introduction to the plate, a piece of paper pressed face down to the stone to transfer the image. This is the early demonstration of chemical lithography and lithographic printing.[51]

In 1825, another major improvement in lithography was invented in France by Joseph Niepce. He had been made experiments with camera obscura and silver chloride papers. He could not manage the problems related with aging and weathering of the silver chloride. By using an alternative substrate -asphalt on tin/pewder plate- he successfully transferred the latent image with camera obscura. Light exposure creates solubility difference and unexposed regions of the asphalt can be dissolved in an organic solvent -distilled rosin, turpentine oil- to create a topographic pattern onto asphalt. This method was named heliography by Niece, which means “writing by the sun” and can be thought as beginning of the modern photolithography.[51]

Today, all electronic devices and gadgets contains a collection of integrated circuits and microprocessors. This branch of technology has developed with a speed unlike any area in human history. Moore's law which dictates the density of transistors in an integrated circuit has doubled in about every 2 years as the density of transistors increases on a circuit and the size of a single transistor become smaller. The capability of fabricating a smaller transistor has deeply been dependent on the developments of the process in photolithography.

Lithographic processes in the semi-conductor industry are quite similar with the Niece's "heliography" in terms of optical pattern translation into a physical pattern. In modern photolithography, exposure sources are highly advanced to decrease resolution of the pattern. Due to physical limitations of the wave-nature of the light, smaller wavelengths must be used for creating devices with smaller features and higher density of production on a limited area. In semiconductor industry, invisible ultraviolet (UV) light (with a wavelength of 365 nm), electron beams, and extreme ultraviolet (EUV, λ=13.5nm) are some of the advanced exposure sources.

The main steps of a generic photolithographic process are; i) Photoresist application (i.e – Spin Coating), ii) Pre-exposure bake (soft bake), iii) Image exposure , iv) Post-exposure bake (hard bake), and v) Development of the resist

The most common resist coating application is spin coating. In the order of millimeters of photoresist is dropped with syringe-like delivery system or using a dropper. The wafer is spun at high speed according to type of the photoresist to coat the wafer uniformly. While spinning continues, wafer is hold from downside with a vacuum. In the method adhesion promotion is very essential. The resist coating will not uniformly spread, will not cover the entire surface, or will have many defected areas without proper adhesion. To ensure the quality of the coated resist, wafer surface must be cleaned with piranha solution (sulfuric acid and hydrogen peroxide mixture) to remove any organic material.

This cleaning step is typically followed by an annealing step to remove any remaining contaminants and dispel any dangling hydroxyl bonds. The substance used for adhesion promotion depends on resist type. For instance, organic based photoresists require a hydrophobic surface to adhere successfully while for aqueous resists need hydrophilic surface. Hexamethyldisilazane (HMDS) is often used to create a hydrophobic adhesion layer between photoresist and silicon. On the other hand, the wafer can be introduced again the piranha solution or oxygen plasma to create a hydrophilic surface.

Silicon wafers have typically a native oxide layer on the surface which is the main reason of the hydrophilic surface character. Firstly, the surface of the wafer needs to be dehydrated to match better with the chemistry of the photoresist in the microfabrication processes. On the native oxide layer, there is an adsorbed water layer due to the ambient humidity. Dehydration step is performed at around 110-120°C in nitrogen environment or ideally in the vacuum. After the dehydration, the surface has still hydrophilic characteristic due to native oxide layer (Si-OH bonds). HMDS treatment must be applied to the surface for desired hydrophobicity. HMDS is reacted with hydroxy groups producing ammonia gas as a side product and complete adhesion promotion step. Successful adhesion promotion heavily depends on dehydration of the surface.

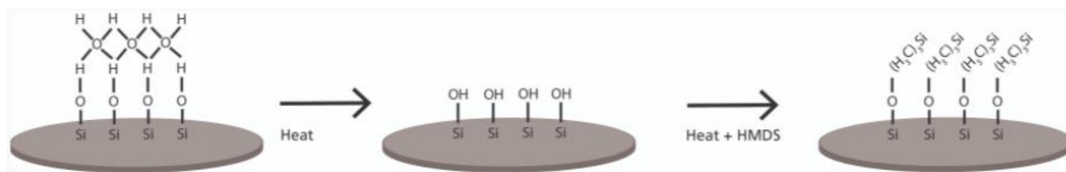

Figure 8 - Adhesion Promotion for Silicon Wafer

After adhesion promotion, photoresist material is coated onto wafer with spin coater. Speed of the rotation and its duration is crucial for the resultant photoresist uniformity and thickness. The optimal rotation speed and the duration of it is provided from manufacturers of the photoresists according to desired thickness and

subsequent fabrication steps. Since photoresists have significant importance in semiconductor industry, their exact compositions are trademarked. However, the fundamental method of creating a solubility difference with energy exposure is still valid.

Most of the photoresists composed of organic polymers and resins mixed with a photosensitive molecule. With light exposure photoresists either become soluble or insoluble in another solution which is called developer. In other words, the polymer resin itself is either insoluble or soluble in the developer solution. Light exposure to the photoresist activates locally photosensitive molecule in it. Activated photosensitizer molecules either enhance or decrease solubility of the polymer resin by reacting it.

Historically, modern photoresists and old blueprint technology is closely related. Blueprints that use diazonium coated papers were one of the first marketed product which based on photo sensitive organic compounds. Blueprint papers have been placed under an opaque mask for sunlight exposure to decompose diazoquinone. Subsequently, ammonia treatment produces diazomium salts from

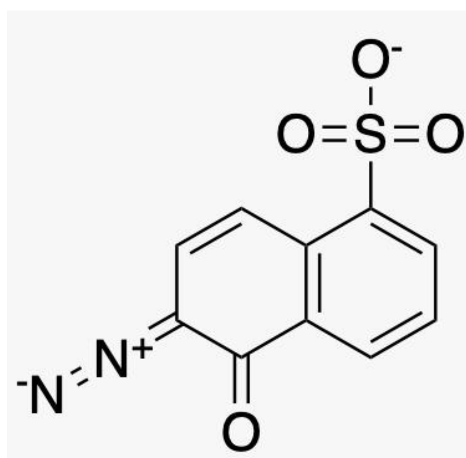

Figure 9-Diazonaphtoquinine - Sulphonate

decomposed diazoquinone molecules by azo coupling agents. The end product forms a blue

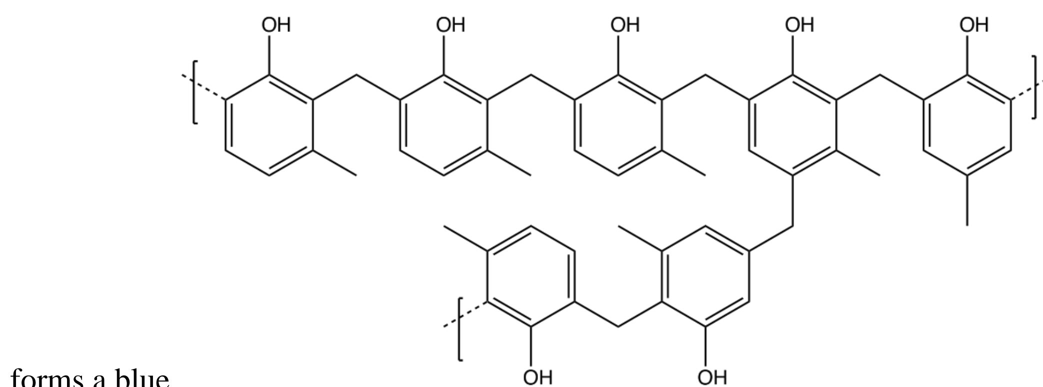

Figure 10 - Novolak

compound and gives the name of the technique. Chemists in Kalle AG -in Wiesbaden, Germany- were experimenting with different diazo compounds to advance the blueprint papers. Oskar Süss, a leading chemist at Kalle AG, has discovered a significant solubility difference in Novolak (a phenol-formaldehyde condensation polymer) and diazonaphthoquinone mixtures in alkali solution. Single phase Novolak (*mentioned as Phenol Resin in the Figure 11*) is quite soluble in alkali medium, but minute additions of diazonaphthoquinone derivatives (like DNQ-sulphonate or DNQ-5-sulfonic acid ester) the development rate (dissolution rate) in the alkali solution shows a dramatic decrease. Because of this solubility difference, DNQ-sulphonate group in the mixture also called inhibitor. During exposure of the novolak resin + DNQ-derivative mixture with an UV source (often with i-line (365 nm) or g-line (435nm) of a mercury lamp), the DNQ is converted into a carboxylic acid as a result of the reaction of nitrogen elimination with a binding water molecule. This structural change causes a sharp increase in alkaline dissolution rate of the PR, makes it highly soluble, even higher than alkaline solubility of pure novolak resin. This sharp change in the solubility, makes possible

photolithography technique in the semiconductor industry with the core principle of Niepce’s “heliography” which is mentioned before. [51]–[53]

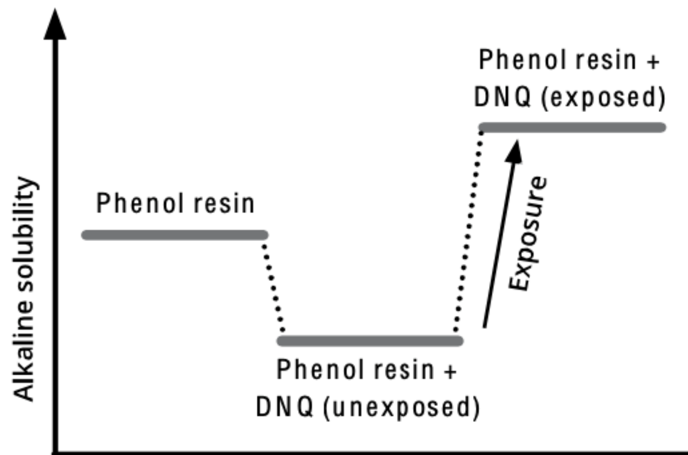

Figure 11 – Solubility diagram of the photolithographic process[54]

To this part, the material selection of the photoresists and some historical aspects of the selection is mentioned. In Figure 12, the main steps of the photolithographic process with a positive tone photoresist are indicated.

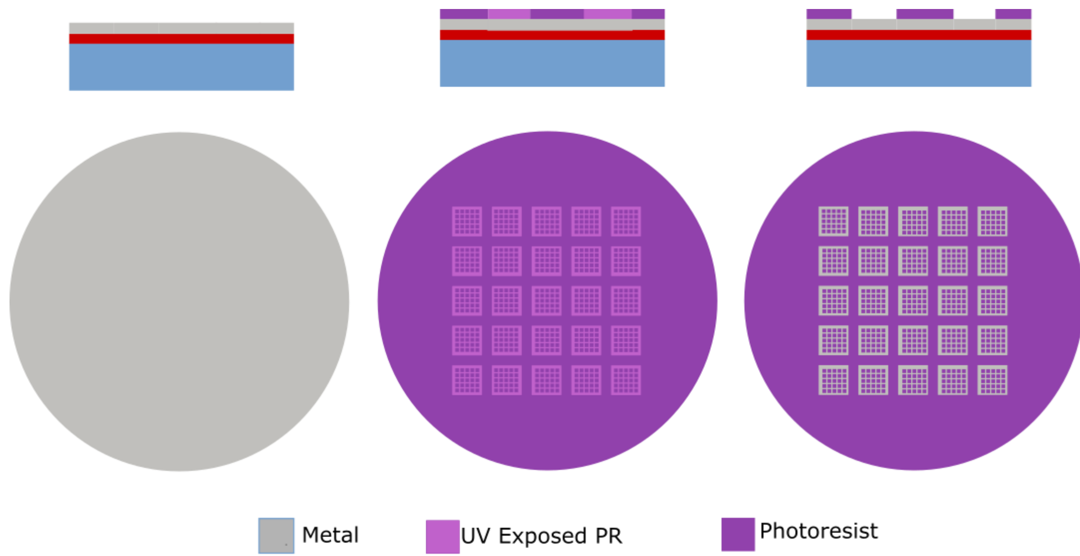

Figure 12 - Transferring a pattern on the metal layer with a positive tone photoresist

i) This step is consisting of adhesion promotion with HMDS and PR application with spin coating. Spin speed controls the final thickness of the PR layer. Thickness information of the resists provided by the manufacturers, and it heavily depends on parameters like molecular weight, average chain length and viscosity.

ii) Soft baking is the step for low temperature (100 °C) solvent evaporation to make the PR layer denser by driving off the excess solvent. Less solvent and denser PR ensures the maximum resolution in the feature size by preventing shape distortions during the exposure. Also, allows complete exposure of the PR down to the below layer

iii) Image exposure is the step for creating a solubility difference in the PR material exposing it with a pattern via a mask or a diffraction pattern. This step has significant importance on the resolution of the fabricated layer. Resolution can be formalized by the Rayleigh equation:

$$R = k_1 \frac{\lambda}{n \cdot \sin \theta_{max}}$$

(Equation 3)

In here, R represents the minimum resolution (same unit with the wavelength of the light), k_1 is a constant unique to the lithographic process (has no unit and is typically in the range of 0.5 –1.0), λ is the exposure wavelength, n is the index of refraction of the medium between exposure source and resist (unitless), and θ_{max} is the maximum half-angle of light that can enter the lens. (also, unitless)

Rayleigh equation shows numerical and unit dependence of the resolution to directly the wavelength of the incident light. The need for faster devices and the demands of the micro transistor industry as indicated in the famous Moore's Law, have pushed forward that projection technology, with a speed unlike any other technology in the history of humankind. Today, sub-5 nm fabrication facilities produce higher speed chips with high energy efficiency thanks to developments in photoresist and projection technology.

iv) Post-exposure bake (PEB), also known as hard bake, is the step that involves moderate temperature treatment (100-150°C) after light exposure. This step may have several functions depending on the PR type and subsequent process steps during microfabrication. For instance, wet etching processes require PEB for better durability in acidic and mildly basic environments. Also, other severe etching or patterning steps like reactive ion etching (RIE) that involves collisions with energetic ion bombardments require PEB for better durability of the PR. However, that last application requires a hard bake, after the development step.

v) The development step is the step in which the PR layer is patterned with the projected image during the image exposure. Depending on the chosen PR material, the final pattern is formed. There are two main general types of PR in that sense; positive and negative photoresists. Positive PRs become soluble with the UV exposure, which means shadowed areas by mask in the light exposure will remain on the wafer. On the other hand, negative PRs become insoluble with the light exposure via crosslinking reactions and the reverse image of the shadow (mask) pattern will be remained on the wafer while the transparent pattern in the mask remained as hallows in the PR layer. Indeed, development solutions and development time have a significant effect on the final surface pattern. The typical development solution is low

concentration TMAH solution (2-3 weight%) which is a mild alkali solution.

2.2 Fabrication of Effective Medium Thin Films

Fabrication steps can be followed from the Figure 13 step by step which is show top view of the structures and cross-sectional layers (along dashed arrows).

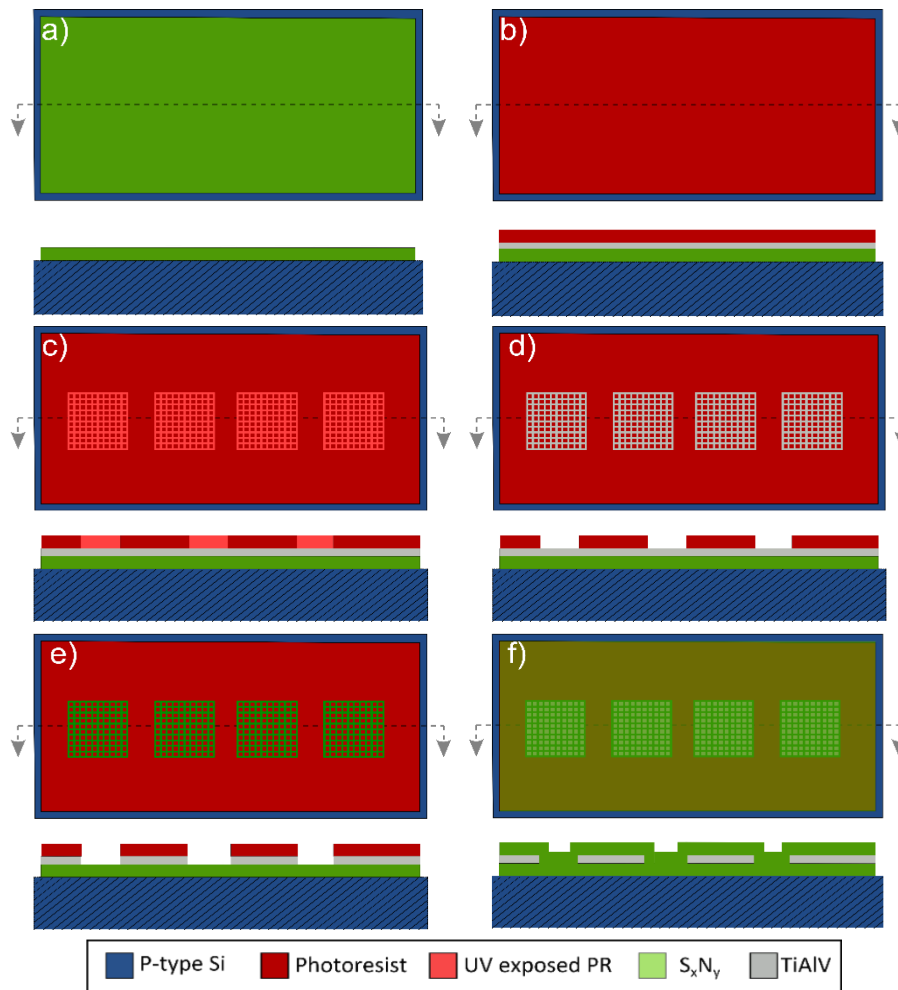

Figure 13 – Schematic fabrication steps of the patterned thin-film structures (Top and Cross-sectional view)

Step 1 – Figure a: A thickness of 20 nm of Si_xN_y was deposited on a 8-inch P-Type silicon wafer by using Plasma Enhanced Chemical Vapor Deposition (PE-

CVD). In this step, silane and ammonia gases reacted in a plasma environment to produce dielectric thin film layer of the effective medium thin films. The reaction between silane and ammonia has an activation barrier which normally can be broken in around 1000°C. In a PECVD chamber, reactants undergo the reaction in the argon plasma environment. Accelerated argon ions provides necessary energy to break activation barrier in kinetic energy form. Hence, the reaction that produces Si_xN_y can undergo in 300 °C successfully, which is favorable in terms of microfabrication ease and compatibility. The final thickness of the coated dielectric layer was verified optically by using FILMETRICS-thin film analyzer.

Step 2 – Figure b: A thickness of 30 nm TiAlV layer (90/6/4 %wt) deposited on Si_xN_y layer with AJA confocal sputtering systems. The sputtering target has dimensions 100 mm diameter (4" inches) and 6.35 mm (0.250 inches) in thickness. The chamber pressure was 3 mTorr and Argon flow was 30 sscm. The deposition rate of the system was 7,2 nm/min that measured with Veeco Dektak Surface Profiler (250 seconds of coating time results with 30,5 nm thin film thickness).

Step 3 – Figure c: A novolak-DNQ based positive photoresist (ULTRA-i™-123) was spun on a spin coater with 3000 rpm for 30 seconds. The term of "positive" means the photoresist became soluble in developing solution after it interacts with UV light and it refers the type of the PR in terms of its reaction to the light interaction. (In negative PRs, regions that are exposed to the light become insoluble)[53] In lithography part, UV light was blocked by using a Chromium mask which is reversely patterned with respect to our desired pattern structure. By using a Stepper Exposure System, (ASML - PAS 5500/200) desired repetitive patterns transferred to photoresist. The exposure power was 400 mJ/cm^2 and wavelength of the UV was 365 nm.

Step 4 – Figure d: Shadowed parts of the PR remained insoluble in the developer solution (Tetramethylammonium hydroxide-based solvent) pattern transfer were completed after developing part.

Step 5 – Figure e: TiAlV wet etch was completed with dipping patterned wafer to the alkali solution in 20 seconds. Alkali solution mixture was prepared with 1500 ml deionized water, 2000 ml hydrogen peroxide, and 500 ml ammonium hydroxide. Water content of the mixture was added to decrease etch rate of the solution. In this step 10, 15, and 20 second trials were performed but the one with 20 seconds was the optimum one in terms of the dipping duration of the wafers into the prepared alkali mixture solution.

Step 6 – Figure f: Another Si_xN_y layer was also coated on the wafer for completing effective medium and as passivation layer. This step is same with step 1 in terms of reaction conditions and reaction time.

Pattern types of the fabricated films can be seen in Figure 14

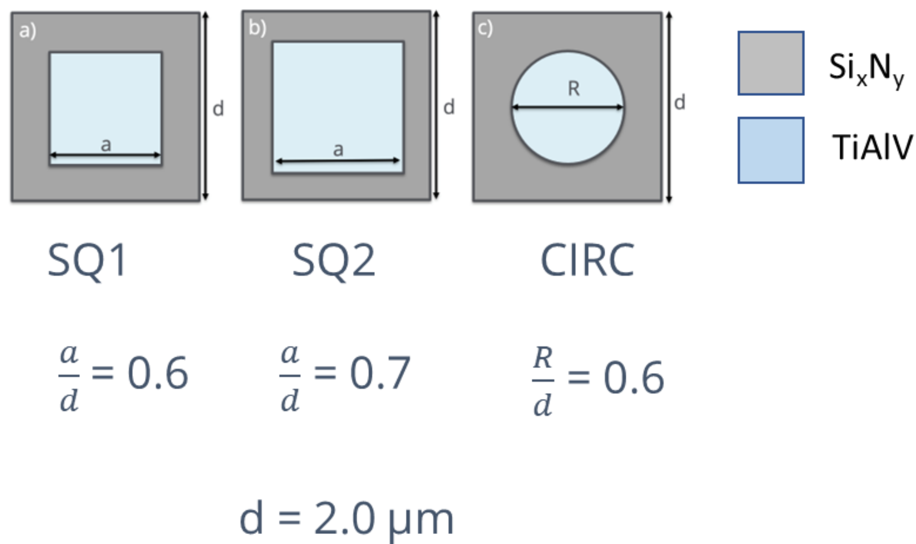

Figure 14 - Unit cells of the patterned thin-films

In the Figure 25, optical microscope images of the effective media can be seen. Especially, square-shaped surfaces have rounded edges and corners than expected. This can be seen also in detail in SEM image of the thin film. Because of the

isotropic etch direction of the etchant solution, corners of the metal parts could not be protected from the wet etchant, and this causes

2.3 Terahertz Characterization

2.4 Terahertz Time Domain Spectrometer

Terahertz time domain spectroscopy (THz-TDS) is the primary characterization method in this study for determination the optical response of the microfabricated thin-films. The system which used is a home-made setup[9] and a transmission system. That means, the transmitted pulse through the sample is detected. However, the emission and detection of the THz signals is not a straightforward task. The THz pulse is generated using a visible Ti:Sapphire pulsed laser beam with 80 fs pulse width and 800 nm central wavelength (Coherent Mantis) and focused on a low temperature grown GaAs (LT-GaAs) photoconductive antenna (BATOP, iPCA-21-05-1000-800-h) Excited structure of the GaAs photoconductive antenna by 800 nm laser produces THz waves in the frequency region from 0.1 to 4 THz. The PCA is gated at a bias voltage of 15 V and 8 kHz modulation. The generated THz beam is collimated, focused on the sample, and collimated again by using off-axis parabolic mirrors in an 8F configuration in a humidity-free environment. After the sample, the beam is focused to a 500 μm thick <110> ZnTe crystal (MTI Corporation) and detected using electro-optic detection methods with a balanced photodiode, lock-in amplifier, and a Wollaston prism. The balanced photodiode and lock-in amplifier are used to record changes in the polarization components of the visible laser beam due to the THz waveform using phase-sensitive detection methods. Both sample and reference measurements are recorded in the time-domain and subsequently analyzed in the frequency domain. All measurements are performed in a humidity-free environment that is achieved by enclosing the system in a box and purging with dry air. THz-TDS diagram used in these measurements is given in Figure 15.

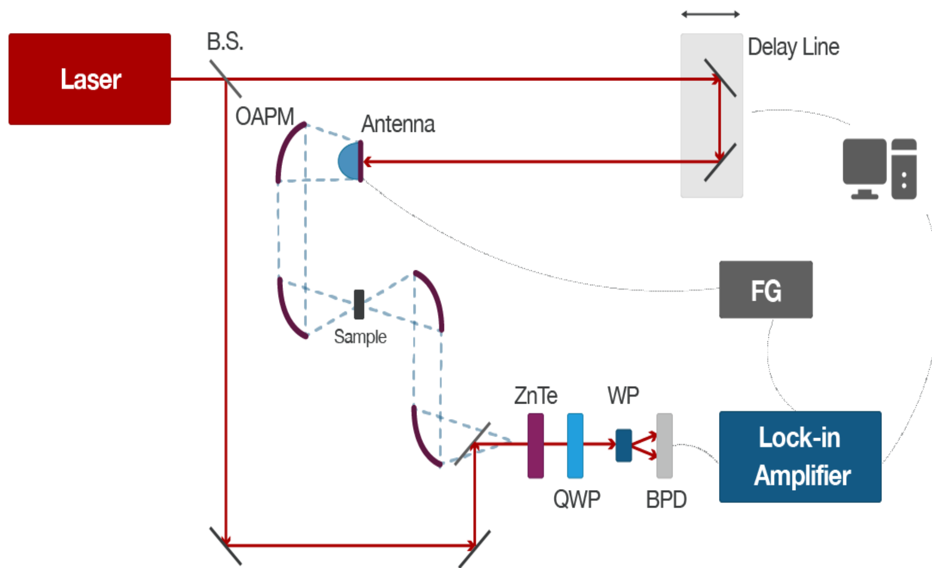

Figure 15 - Schematic Diagram and the Photo of the home-made THz-TDS Setup[9]

Using time domain data, equal numbers of data points converted into frequency domain by using Fast Fourier Transformation (FFT). Parameters of the conversion can be seen in the Figure 16.

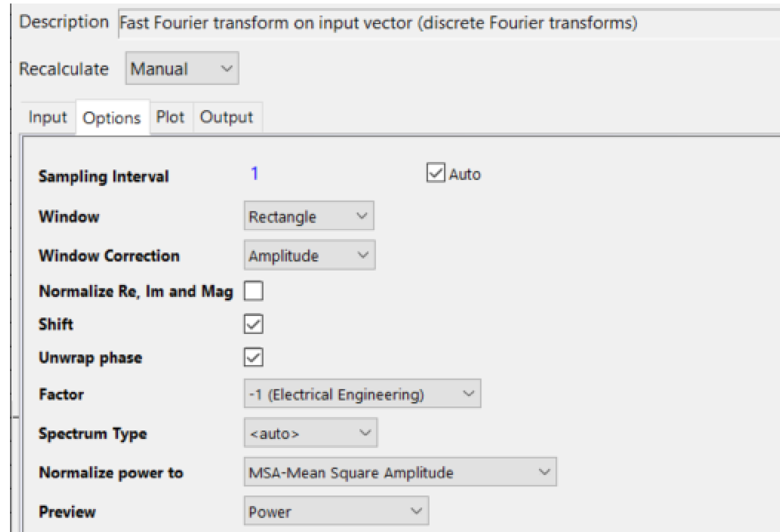

Figure 16 - FFT parameters that used in the Origin Pro Software

CHAPTER 3

RESULTS & DISCUSSION

In this chapter, all results collected through this study and fabrication details are reported and discussed. In the first part, samples of SQ1, SQ2 and, CIRC films are compared with the non-patterned peers that are fabricated on the same wafer and influence of the etch time during pattern transfer is shown. In the second part, the relationship between the spectral transmission level and volumetric metal content of the thin films is investigated. In the third part, the influence of annealing on the THz response of the fabricated thin films is shown. Next, our simulation results and spectral response of the fabricated thin films compared in the 0.1 and 1.0 THz region are discussed. At the last part, calculated refractive index and extinction coefficients of the SQ1 sample are presented.

3.1 Preliminary Works

Before initializing the fabrication of the effective thin-films and the microbolometer pixel, deposition parameters of the metal (sputtering) and the dielectric layers (PECVD) were determined. Also, wet and dry etching parameters have been determined. This section summarizes determination of microfabrication parameters.

3.1.1 Optimization of the Thickness of Dielectric Layer

According to preliminary simulation results, optimum metal content of the effective medium thin films determined as 33% volumetrically. Response time of the sensor and total thermal mass is inversely related with each other. To have coating of a

continuous thin-film, dielectric Si_xN_y layers of the first trial had kept around 45 nm. So, despite we detect an optimum metal content level as 33% volumetricallyin theoptimization part, metal content of the first thin films is around 10% volumetrically because of the fabrication ease.

First, an 8” p-type Si wafer is cleaned with Radio Corporation of America (RCA) procedure (5 min of piranha solution exposure for organic contaminants and 37% Buffered HF exposure for oxide cleaning for 10 mins) . By using PECVD coating system, with silane and ammonia gas, during 187 secs, SixNy was coated on the cleaned wafer. (Measured thickness is around 45 nm) Since this method ends up with a non-stoichiometric coating, Silicon Nitrate referred as SixNy during this study. Thickness of the coated dielectric thin films measured with FILMETRICS thin film thickness analyzer and justified with cross-sectional SEM imaging.

3.1.2 Optimization of the Thickness of the Metal Layer

Sputter deposition parameters are determined for optimum non-uniformity on the 8” wafer for coating same thickness of metal for all fabricated thin films. To reduce the non-uniformity level below 10% between extremum points of the wafer, distance between target and the substrate were optimized. In this study, AJA Orion 8 series sputtering system was used. This equipment has an in-situ gimbal for targets with 4” (10 cm) diameter to tune the angle between the substrate and the

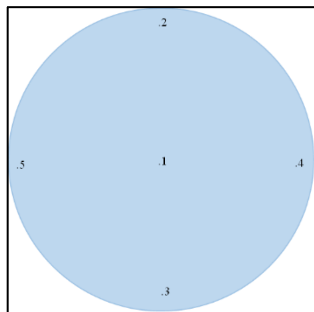

Figure 17 - Numeric Labels of the measured areas of the 8" Wafer

target. During optimization studies, chamber pressure was kept in 3 mTorr for deposition. Coating time was 600 seconds with 120 seconds shutter delay for

plasma stabilization. Applied DC power was 400 W and ramp time for that power was 120 seconds.

Coated 8” dummy wafer with some features that shadowed and exposed to the UV light in some areas investigated with Veeco Dektak 8 Surface Profiler. During the thickness measurement, applied force at the contact stylus was 3 mg. Measured thickness values are reported at the Table 1.

Table 1 - Thickness values of Patterned TiAlV layer on the numbered areas of an 8" Wafer

Point #	Thickness at Die #1 (nm)	Thickness at Die #2 (nm)
1	44.5	43.7
2	43.0	41.7
3	42.3	42.3
4	41.0	41.2
5	42.1	43.1

The results showed that our wafer level non-uniformity level was 7% for the 44.5 nm metal layer. The maximum thickness difference was measured as 3.5 nm with the center of the wafer (point #1/die#1) and the right-hand side (point#4/die#1) of the wafer.

3.1.3 Optimization of the TiAlV Etch Process

Pattern transfer onto the wafer was completed with etching of the coated metal layer. While desired places are protected with photoresist, open areas on the wafer introduced to wet etchant solution in the wet etch trials. Also, plasma assisted dry etch method was tried in this study.

In wet etch optimization studies, ammonium hydroxide and hydrogen peroxide mixture were used. This mixture is used for titanium etch in the microfabrication. Since our coated TiAlV layer consists of Ti 90% in weight, it is seen as a suitable

etchant for our application. In the first trial, NH_4OH and H_2O_2 mixture was prepared in 4:1 ratio in total 4000 ml. However, reaction occurred aggressively and caused damage in the protected areas. In the Figure 18, over-etched areas can be seen in naked eye and in 150x optical zoom.

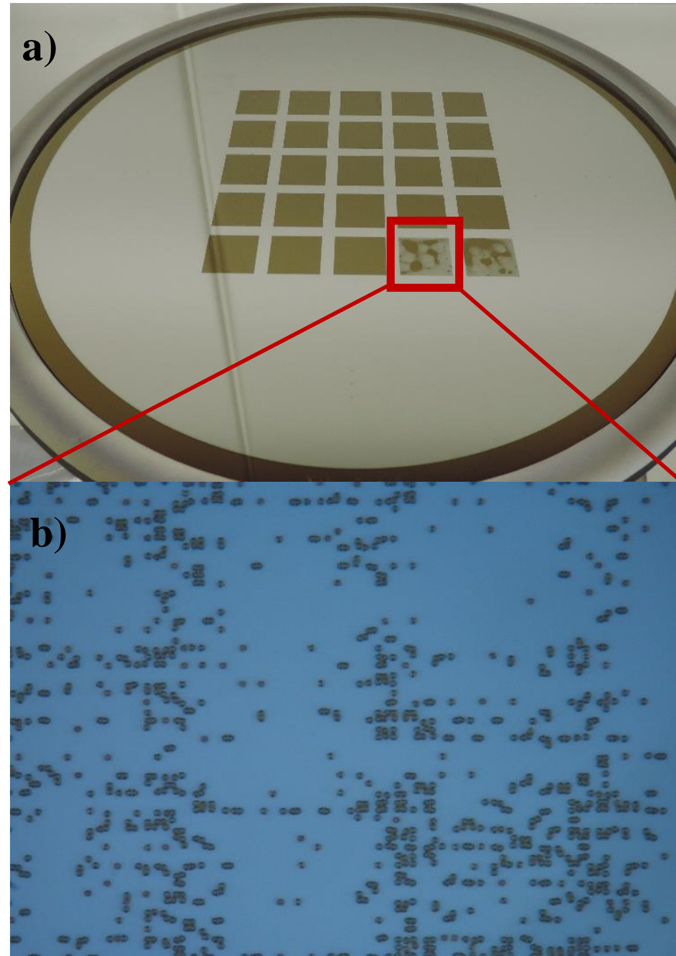

Figure 18 - Over-etched thin film with die number #24 in a) naked eye and b) 150x optical zoom

After this unsuccessful trial, etchant solution was reprepared with water addition with in 1:4:3 ratio of NH_4OH:H_2O_2:H_2O in total of 4000 ml. To this diluted etchant, three separate refabricated wafers introduced with dipping for 10, 15, and 20

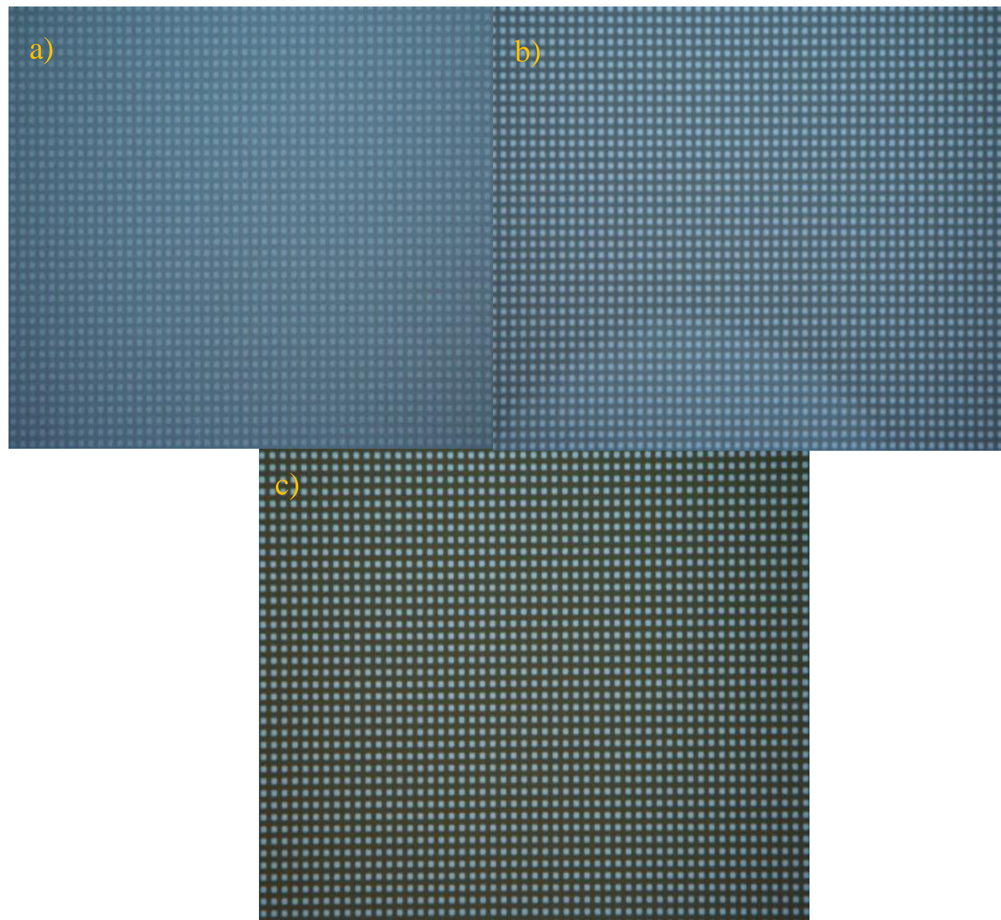

Figure 19 - Optical microscope images of a) SQ1-10s

b) SQ1_15s, and c) SQ1_20s

seconds. Among these wafers, the one dipped for 20 seconds was the best. This observation is also verified with THz measurements (please see page 43). In the Figure 19, etch time comparisons can be seen for 10 seconds, 15 seconds and 20 seconds.

3.2 SEM-EDX Characterization

In the production of TiAlV thin films, a single target material "TiAl6V4" (Kurt J. Lesker Company) was used in alloy form. The element ratios in the films produced by the direct current sputtering deposition technique were determined by SEM-EDX analysis from the cross-section. The cross-sectional SEM image of the produced film and the point where the EDX analysis was performed are shown in Figure 20.

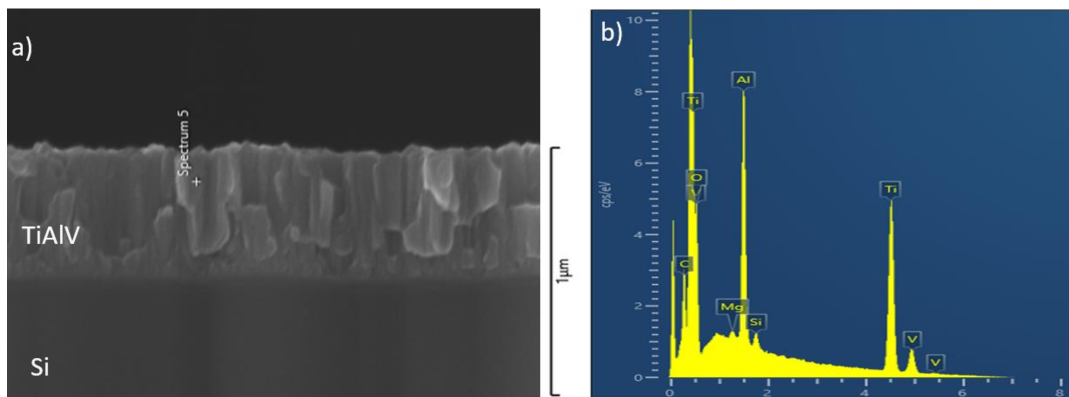

Figure 20 - a) Cross-sectional SEM of the TiAlV layer b) EDX analysis spectrum of the TiAlV

When these ratios were compared with the ratios of the target material, it was observed that the element ratios of the grown film and the target material were compatible (See Table 2).

Table 2 - Elemental ratios in the thin film coated with the element ratios in the target material

Element	Sputter Alloy Target Ratios (Kurt J. Lesker) (wt. %)	EDX Results (wt. %)
Ti	90	88.7
Al	6	6.9
V	4	3.8

Fabricated thin films are examined in vacuum environment by using SEM-EDS characterization method (Hitachi Regulus 8230). Titanium content of the etched areas of the thin films are radiated with X-ray radiation and collected Auger and backscattered electrons are characterized according to their energy levels. Elemental percentage analysis and the SEM image of the SQ2 sample can be seen in Figure 21 and Figure 22.

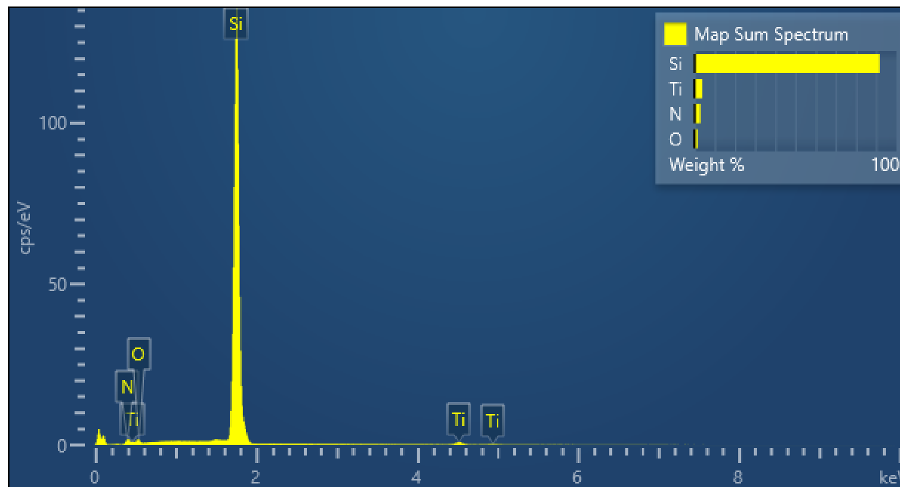

Figure 21 Elemental percentages of the inspected surface

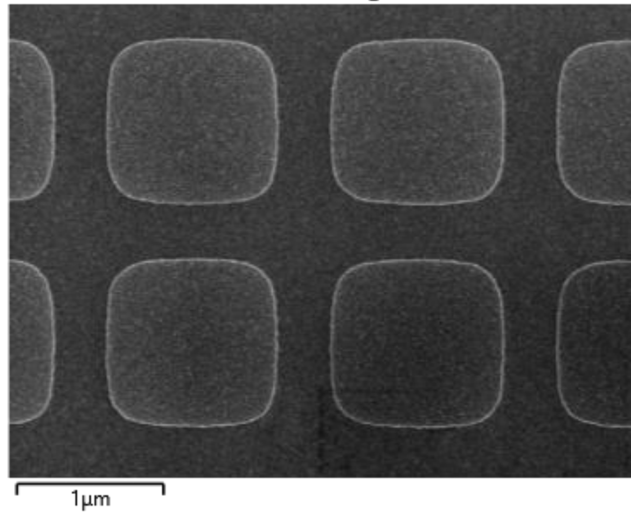

Figure 22 - SEM Image of SQ2 Sample with 30000x magnification

Table 3 - Elemental analysis of the SQ1 sample with SEM-EDS

Element	Wt%	Wt% Sigma
N	2.87	0.18
O	1.48	0.06
Si	91.75	0.20
Ti	3.91	0.09
Total:	100.00	

Element	Line Type	Apparent Concentration	k Ratio	Wt%	Wt% Sigma	Standard Label	Factory Standard	Standard Calibration Date
N	K series	0.02	0.00003	2.87	0.18	BN	Yes	
O	K series	0.01	0.00003	1.48	0.06	SiO2	Yes	
Si	K series	0.54	0.00425	91.75	0.20	SiO2	Yes	
Ti	K series	0.02	0.00015	3.91	0.09	Ti	Yes	
Total:				100.00				

Label:	Electron Image 17
Collected:	9/22/2021 4:39:41 PM
Input Signal:	SE
Resolution (Width):	1024 pixels
Resolution (Height):	768 pixels
Pixel Size:	0.00421 µm
Image Width:	4.31µm
Image Height:	3.23µm
Stage Tilt Degrees:	0.00°
Specimen Tilt Degrees:	0.00°
Software Tilt Correction:	Not applied
Magnification:	30000 x
Number of Averaged Frames:	1
Dwell Time:	5µs

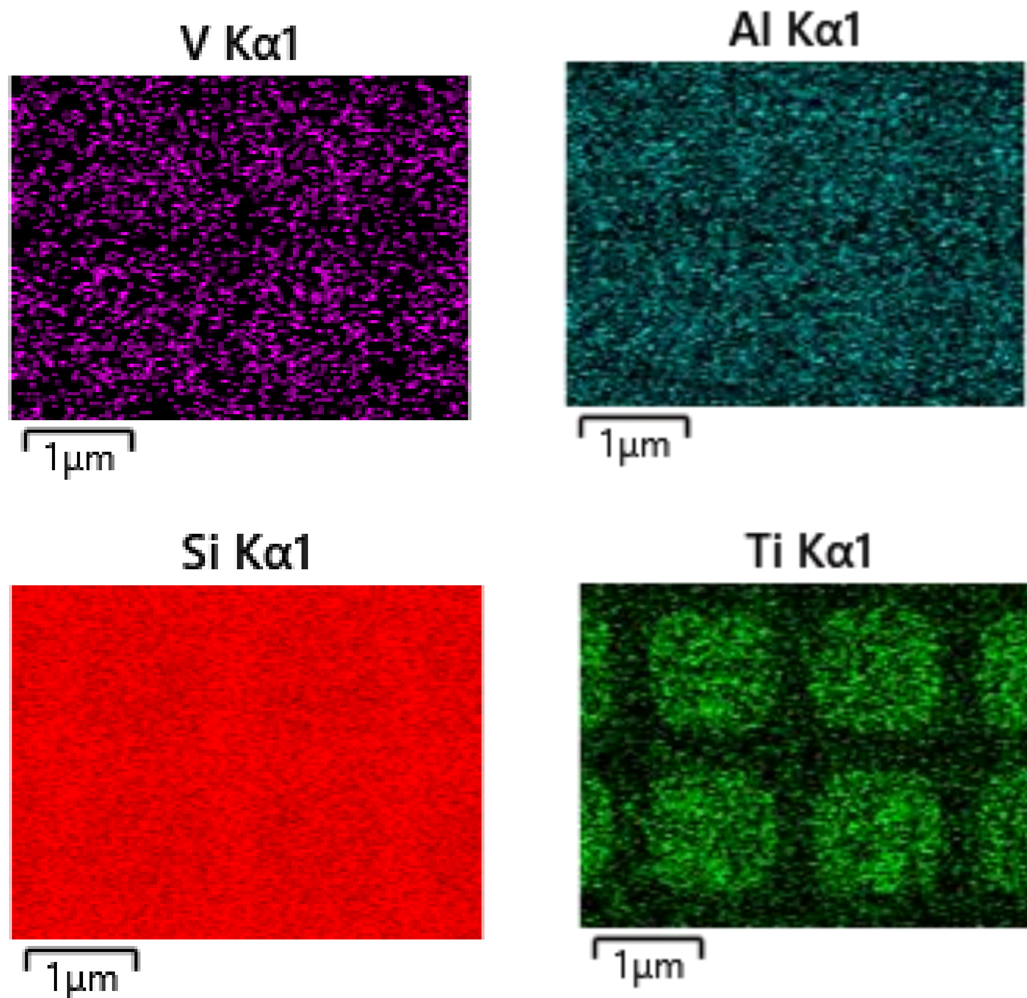

Figure 23 - Elemental map of the EDS Results

As can be seen in the Figure 23, metal etching of the pattern transfer step is validated by using elemental ratio of the titanium metal in the TiAlV content. (Ti:90%, Al:6% and, V:4% by mass). Patterns of the metal layer could not be seen for Al and V. This may be due to insufficient resolution of the SEM-EDS equipment for that level concentration. Also, the structures are masked with SixNy layers and this may hinder the observation of the buried Al and V that are in low amounts. Those factors decrease reliability of the measurement. However, observed titanium map of the patterns is used for rough validation of the plasma etching of the TiAlV layer. Detailed parameter list of the analysis can be seen on Table 3. The areas that protected with photoresist creates metal areas in the spectral map. (Figure

23) Silicon metal percentage dominates inspected area. That is mainly about penetration depth of the X-rays and emitted photons. Due to higher penetration depth of the EM waves with respect to thickness of effective media, the result of the analysis heavily influenced by the composition of the substrate underneath of the effective thin films which consist of silicon. However, spectral images can be used for the rough estimation of the etching step.

3.3 Influence of the etching time on the THz response

Fabricated thin films with patterns by using wet etching are investigated in terms of THz response. Via dissolution of the TiAlV layer at the non-protected parts of the thin film, the pattern transfer is completed. Separate equivalent wafers are dipped into the alkali solution that mentioned in Section 3.1.3.

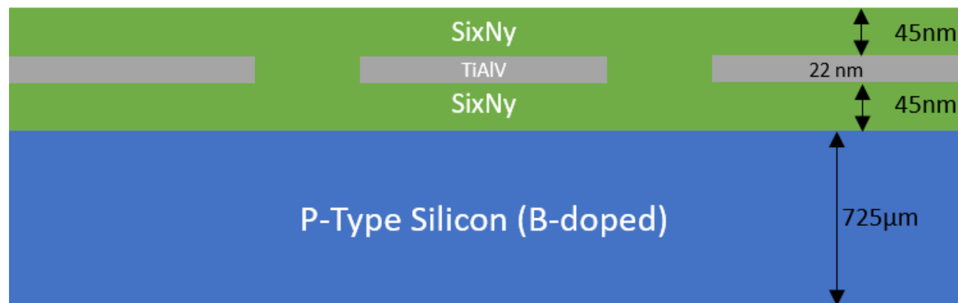

Figure 24 - Cross-sectional diagram of the fabricated thin-films

In the Figure 24, measured cross-sectional thickness with SEM of the thin films are shown. The duration of the dipping to etchant is the only difference in the process flow. (10, 15, and 20 seconds). During the optimization step of the wet etching of the TiAlV, above 25 seconds, pattern of the metal was completely dissolved on the top of the $_xN_y$ layer. That is why 20 seconds are determined as the limit of the maximum etching time for the process.After the thickness and coating parameters are optimized (Details are given in Section 3.1.3), the next step is to measure the film layer resistances. Thin film samples to be produced for electrical measurements were prepared in a way that they could also be measured in the THz

setup in the next step. For this purpose, an 8” Silicon substrate was coated with Si_xNy using plasma-supported chemical vapor deposition PECVD (Plasma Enhanced chemical Vapor Deposition) technique. This Si/SixNy backing was then cut into squares with a side length of 2.5 cm. After cutting, all parts were cleaned with a Q-tip in acetone bath and then in isopropyl alcohol bath, rinsed and made ready for coating. For each different thickness, 3 pieces were selected side by side. The middle piece was separated as a reference and the other 2 pieces were coated. One of the coated parts was used for sheet resistance measurement and the other for THz measurement.

Sheet resistance measurements were made with a 4-point probe system and reported in Table 4. In line with the results, due to increased volume of the electrically conductive TiAlV a decreasing layer resistance was observed as the TiAlV thin film thickness increased as expected.

Table 4 - Thickness vs sheet resistance values of TiAlV thin-films

Coating Time (s)	Thickness (nm)	Sheet Resistance (Ω/sq)
75	7	470
106	10	290
160	15	165
213	20	127
320	30	78
520	49	56
720	68	42
2000	188	17
5000	498	8.9

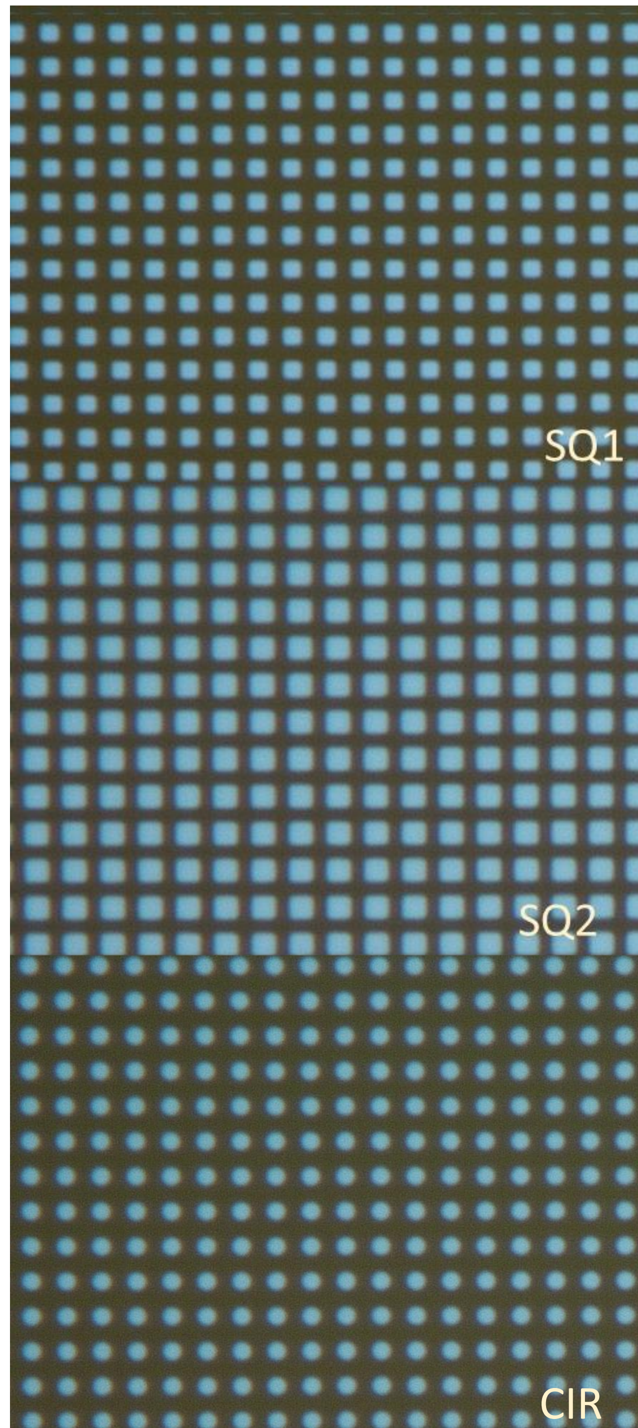

Figure 25 - Optical Microscope images of the patterned thin-films with 150x magnification

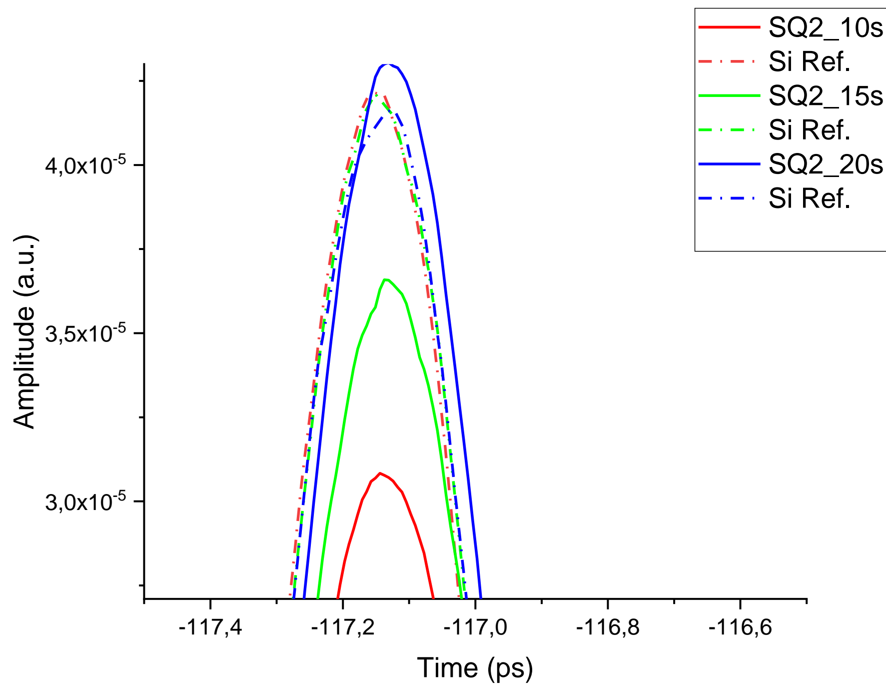

Figure 26 - Peak amplitudes of the THz profile in time domain of SQ2 samples etched for 10, 15, and 20 seconds

Figure 26 shows the change in peak amplitudes of three SQ2 samples obtained with three different etching time. As the etching time increases the metal content of the sample decreases, thus there is an inverse relationship between THz transparency and overall metal content of the thin films. This is expected because of the highly reflective nature of the metals for THz radiation. Interestingly, the sub-wavelength patterns obtained with a 20-second dipping to the etching solution have a similar transparency with non-patterned silicon wafers (our substrate). That may be caused at that level of metal etching (down to below dielectric layer), our repetitive metal structures cannot be seen as bulk metal by the THz waves due its large wavelength with respect to embedded metal structures. In addition, the SixNy is a lower index material thus acts as a anti-reflective coating on the surface of the structures. With 20-second etching the metal content of the thin film is lowered to a level such that

the loss due to metal layer was compensated by the the increased transmission with the anti-reflective coating.

The following figures (27-32) compares the time domain profiles collected with the THz-TDS of the three different fabricated structures of the thin films. With the increasing etching time, THz responses of the thin films start to resemble to THz response of the non-patterned Si substrates. That finding points that, our patterned structures do not show bulk metal properties in the scanned THz region.(0.1 – 2.0 THz) In addition as stated the SixNy layer may be acting as anti-reflective layer. Moreover, there was no significant measured difference between SQ1, SQ2, and CIRC samples in terms of approximate refractive index (based on time delays in peak positions) and also transmission levels. Our overall film thicknesses are below 100 nm for all samples and refractive index difference cannot be detected with our THz-TDS measurements.

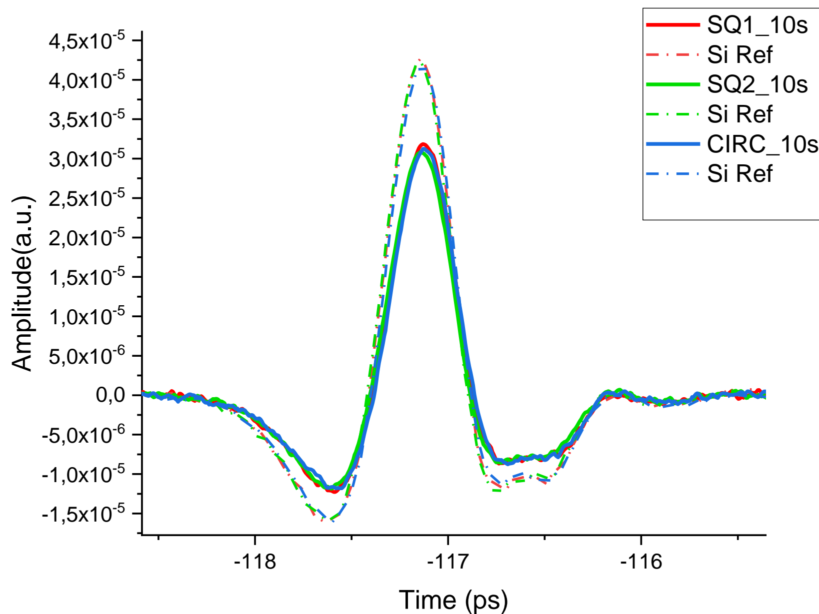

Figure 27 - THz time domain data of the samples with the 10-second dipping to the etchant solution

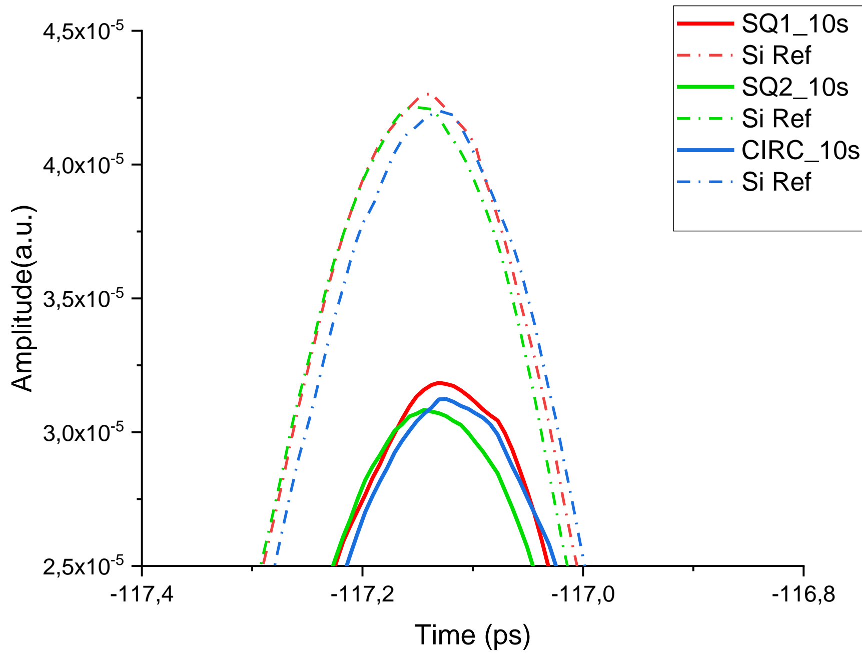

Figure 28 – Magnified version of the Figure 27 to its peak region

As can be seen in the Figure 28, 10 seconds dipping time in the etchant solution decreases amplitude of the transmitted THz pulse through the media for the SQ1, SQ2, and CIRC samples with respect to non-patterned silicon substrate. Since the overall thickness and the number of the interlayers vary through the structure, this result is expected. However, while etching duration increases to 15 and 20 seconds, the difference between amplitudes of the THz pulse becomes insignificant. After 20 seconds of wet etching, transmitted amplitude becomes even higher than just the substrate. As mentione, SixNy layers might be acting as a good anti-reflective coating. Otherwise, our fabricated samples: SQ1, SQ2, and CIRC do not cause any significant difference in terms of THz transmittance. Effect of the etchant solution on the substrate (p-type silicon) via etching in a small rate may be caused a thinning effect and increased THz transmittance. This could be a possible explanation for the nearly same response of the p-type Si substrates and the fabricated thin films.

However, we have also conducted studies on non-patterned SixNy/TiAlV/SixNy films. No significant change in THz transmission with the difference in the thickness of the substrate due to the etching time could be observed. (Figure 33)

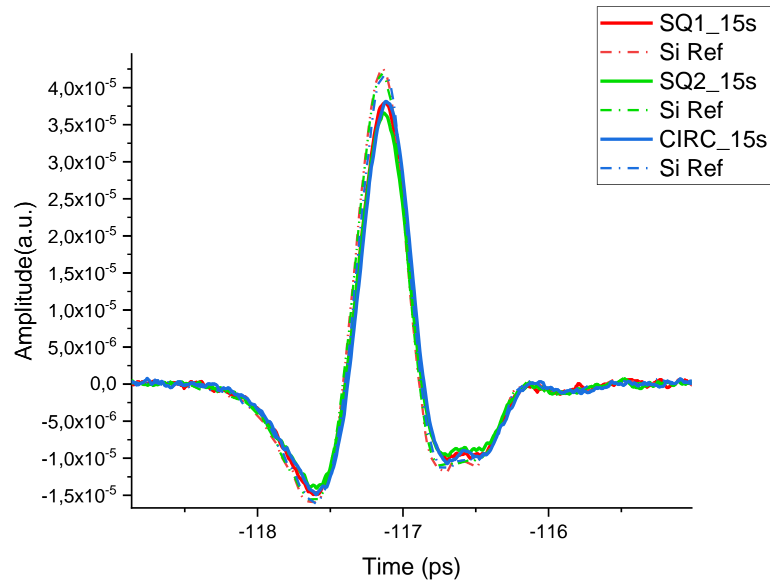

Figure 29 - THz time domain data of the samples with the 15-second dipping to the etchant solution

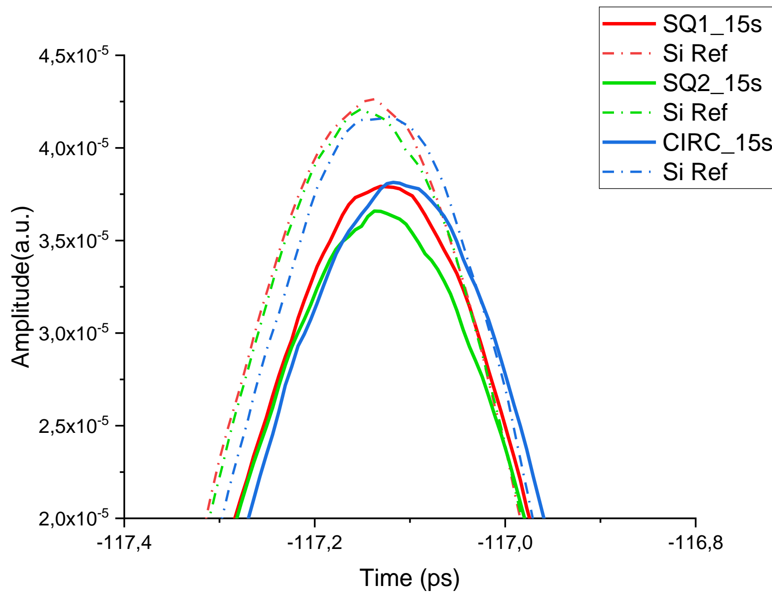

Figure 30 - Magnified version of the Figure 28 to its peak region

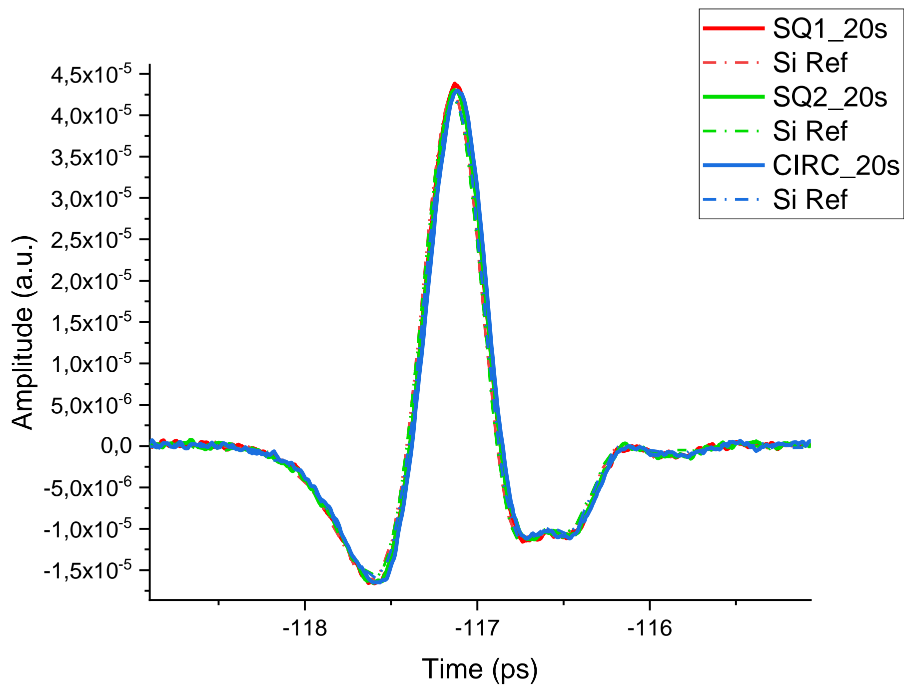

Figure 31 - THz time domain data of the samples with the 20-second dipping to the etchant solution

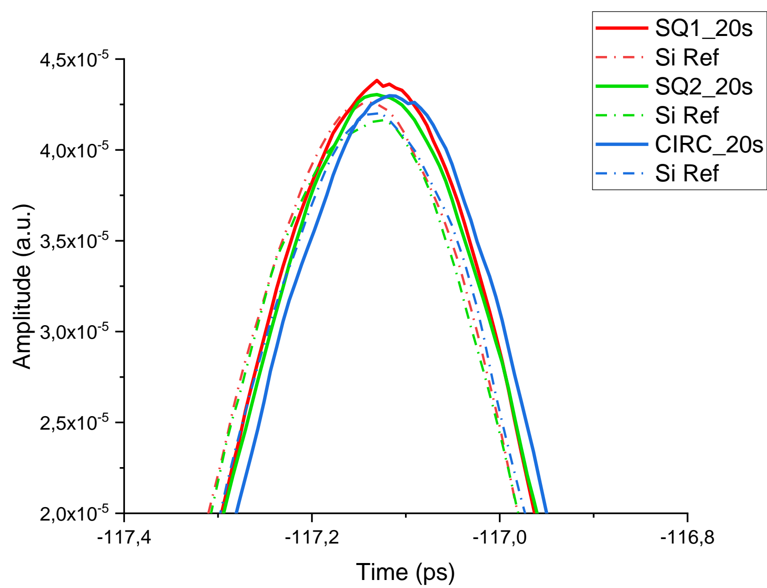

Figure 32 - Magnified version of the Figure 30 to its peak region

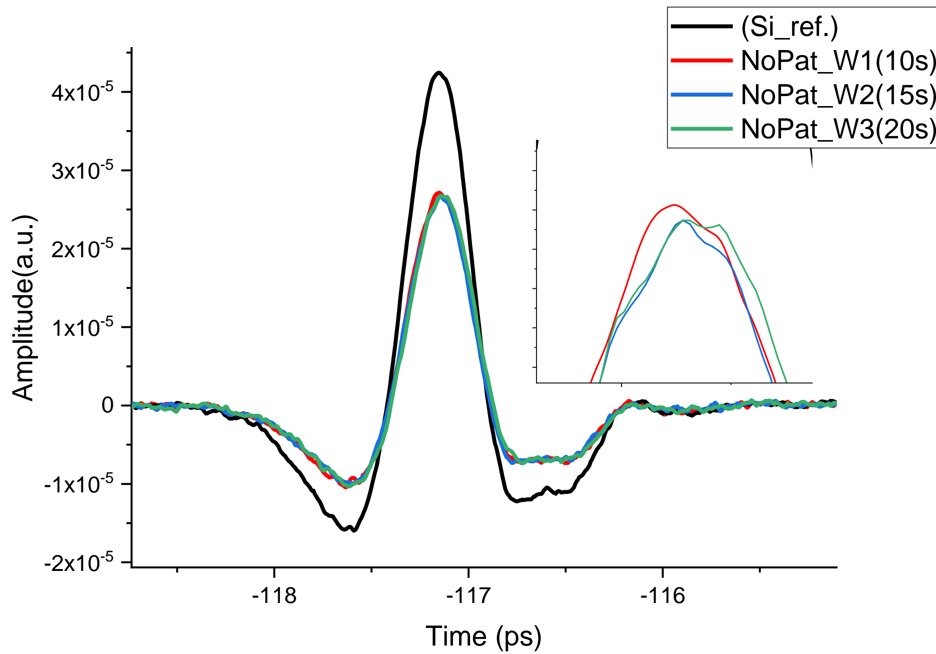

Figure 33 - THz response of the PR protected, non-patterned parts of the wafers after 10,15, and 20 seconds of dipping to the etchant solution

THz response of the photoresist protected non-patterned parts are also characterized. As can be seen in the Figure 33, there is no difference between different etch durations. That is a convincing result in terms of selectivity of titanium etchant solution. The solution does not cause any damage on the backside of the wafer, which has P-type silicon.

3.4 Influence of the Volumetric Metal Content

As explained in Section 3.3, SQ1, SQ2, and CIRC samples did not resulted the effect we would like to see as seen in the THz-TDS measurements. For further investigation, a new production design has been adopted to adjust the metal doping ratios with the microfabrication method. In this new production design, the dielectric height difference on the metal islands used in Bruggeman active media films was successfully produced by using reverse lithography method, without

changing the lithography mask. The new production design method developed is explained in detail below.

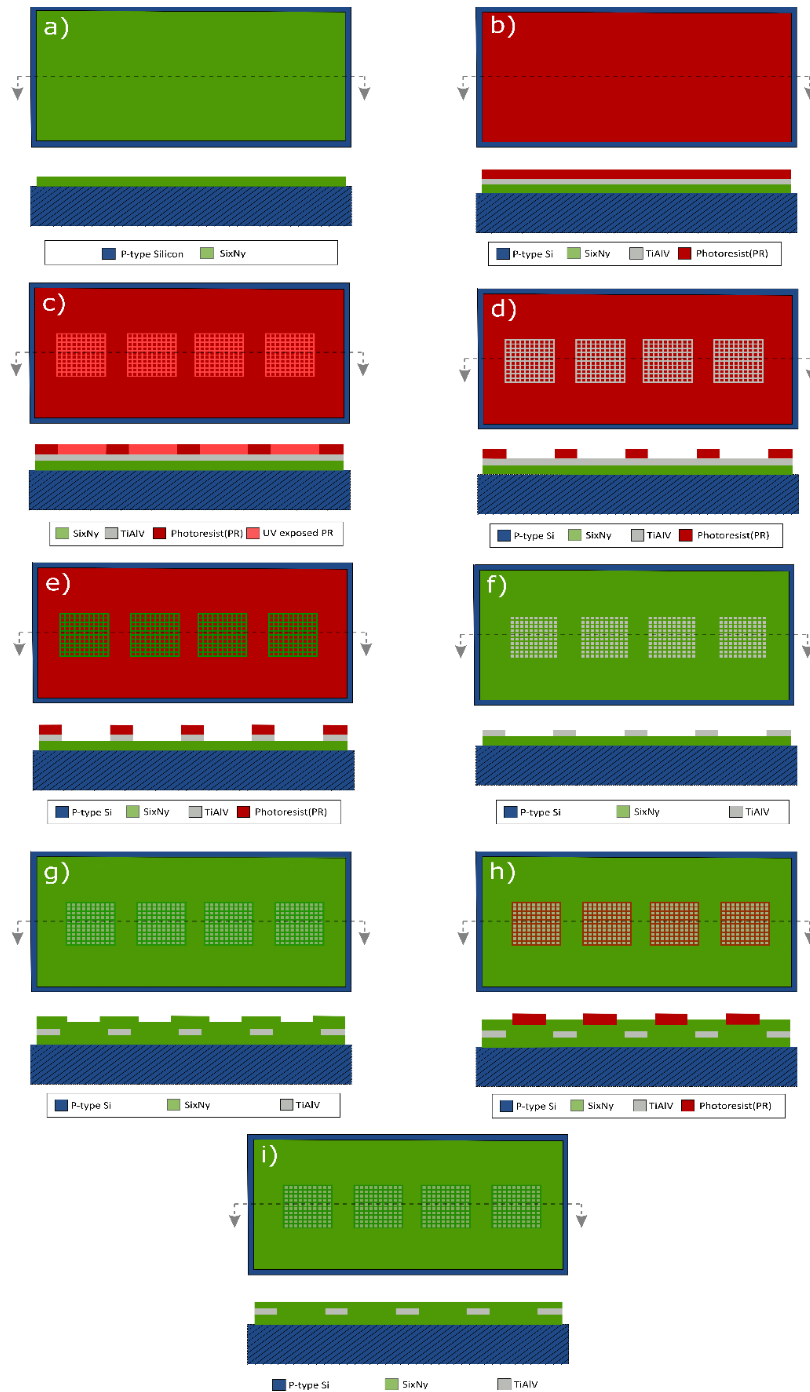

Figure 34 - Schematic fabrication steps of the patterned thin-film structures with higher volumetric metal content (Top and Cross-sectional view)

In Figure 34, the section and top view of the production process is shown schematically. The films were produced on 20 cm (8 inch) Si discs. Si/SixNy layer was obtained by growing the Si_xN_y layer on boron doped Si discs, and the metal active media films to be coated on this base disc were electrically separated from the p-type Si wafer (Figure 34 (a)).

This Si_xN_y layer was grown by PECVD method like previously mentioned. The amount of metal was increased by about 20% compared to the samples presented in the previous section.

The Bruggeman active medium is coated with photoresist (PR) (Figure 34(b)). The PR layer used becomes soluble with ultraviolet light. With the stepper exposure system, the desired pattern is transferred onto the PR with ultraviolet light (Figure 34c)). The ultraviolet parts dissolve with the help of chemical solvent solutions and become spaces between metal islands in the pattern (Figure 34 (d)). While the TiAlV layer was shaped by plasma etching, the insoluble PR parts protected the metal layer underneath, allowing the desired pattern to be given to the metal (Figure 34(e)). Instead of chemical etching of the TiAlV layer, plasma etching was used in the new production process. The biggest reason for this is that the solution during chemical etching reacts more aggressively than expected and the designed metal films remain in a high-resolution structure during patterning due to their thickness. In the new plasma etching method, O_2, Ar and Ar/Cl gas mixtures were passed to the plasma phase under the electrical field, respectively, and the ions formed were accelerated towards the metal layer of the films. As a result of the impact of the ions, the material was removed from the desired surface and abraded. Optimization of the process could be carried out more precisely because the gas flow amount and electrical potential parameters can be changed in addition to the process time. After cleaning the PR layer remaining on the surface of the TiAlV layer (Figure 34(f)), the second SixNy layer was laid with the same thickness and production method as the substrate (Figure 34(g)). At this step, it is seen that the SixNy layer on the metals remains higher and there are level differences. To prevent the incoming electromagnetic waves from being adversely affected by these level differences,

another lithography step has been added to the end of the production plan (Figure 34(h)). First, the parts to be protected are covered with PR. Subsequently, SixNy etching was performed with physical-chemical plasma etching targeting 10 nm etching (Figure 34(i)). This step was carried out by impinging the CF_4/Ar gas mixture onto the surface after the Oxygen plasma step.

In order to increase the final metal percentage to 33%, the production process was optimized and the lower and upper SixNy layers were reduced to 20 nm and 10 nm levels, respectively. The etching time and the success of the process are verified by energy dispersion X-Ray (EDX) spectrometry in Figure 35.

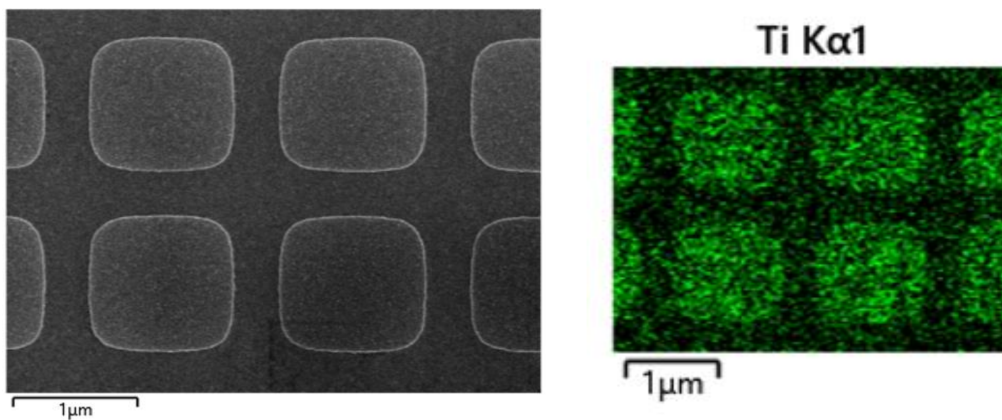

Figure 35 - SEM-EDS Analysis After Plasma Etching, Elemental Ti Analysis Confirmed Etching Complete

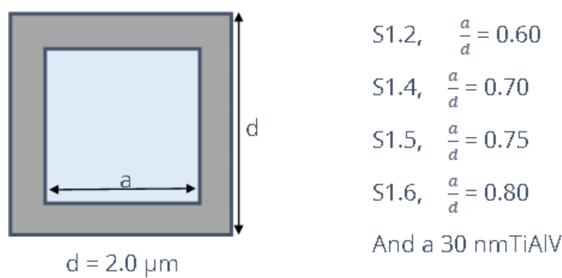

Figure 36 - Images of 150x magnified thin films with higher metal content

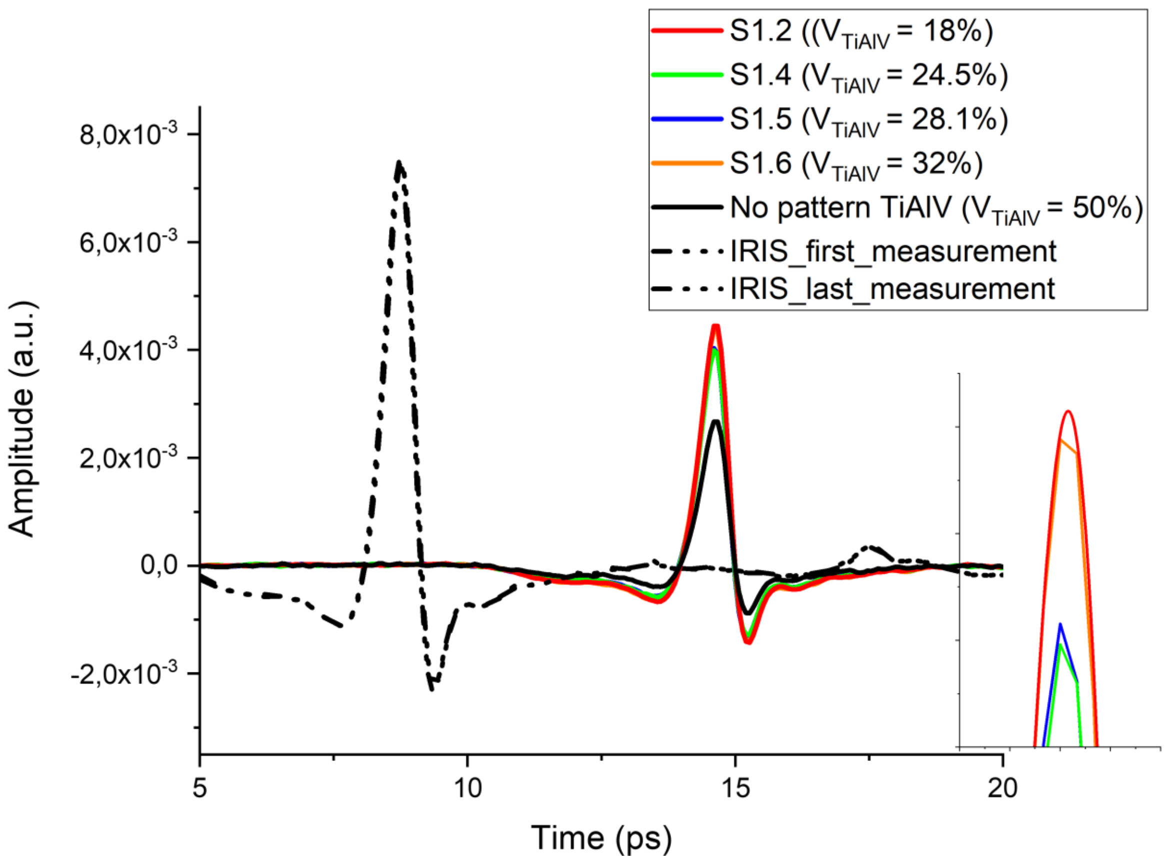

Figure 37 - Time Domain Data of the thin films

with high volumetric metal content

Despite the significant metal content difference of the samples S1.2 and S1.6, their THz transmission is very similar. This can be interpreted as a potential fabrication fault. Because of the that result, those samples were examined with cross-sectional SEM. There was no distinct borders between dielectric and metal components of the thin film, probably charging effects as a result of encapsulated metal layer inside the dielectric. But total thicknesses of the S1.2 and S1.6 are measured as 89.7 and 60.9 nm respectively (Figure 39). That thickness difference can explain the similar THz transmission levels of S1.2 and S1.6. To get a better -uniformity level on the wafer, further optimization studies are needed.

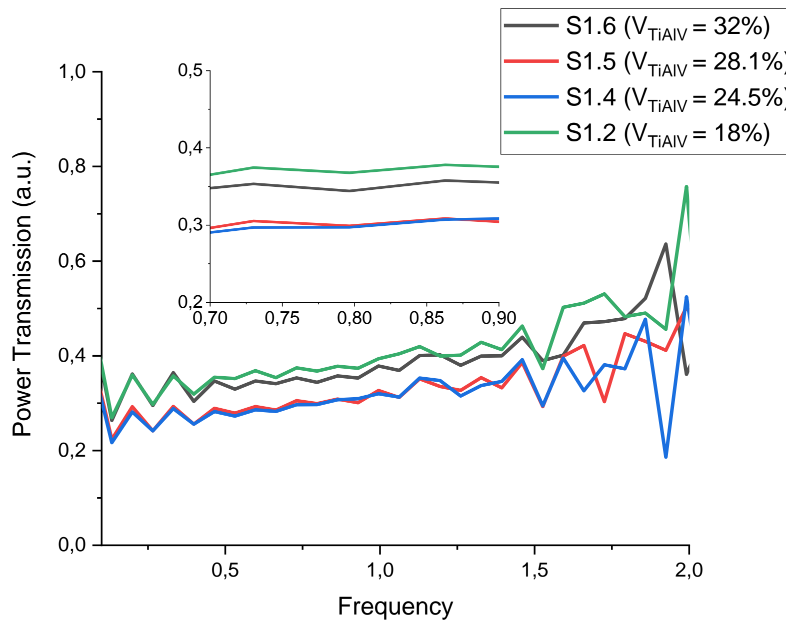

Figure 38 - Power Transmission data of the thin-films with higher metal content (with respect to air - through iris-)

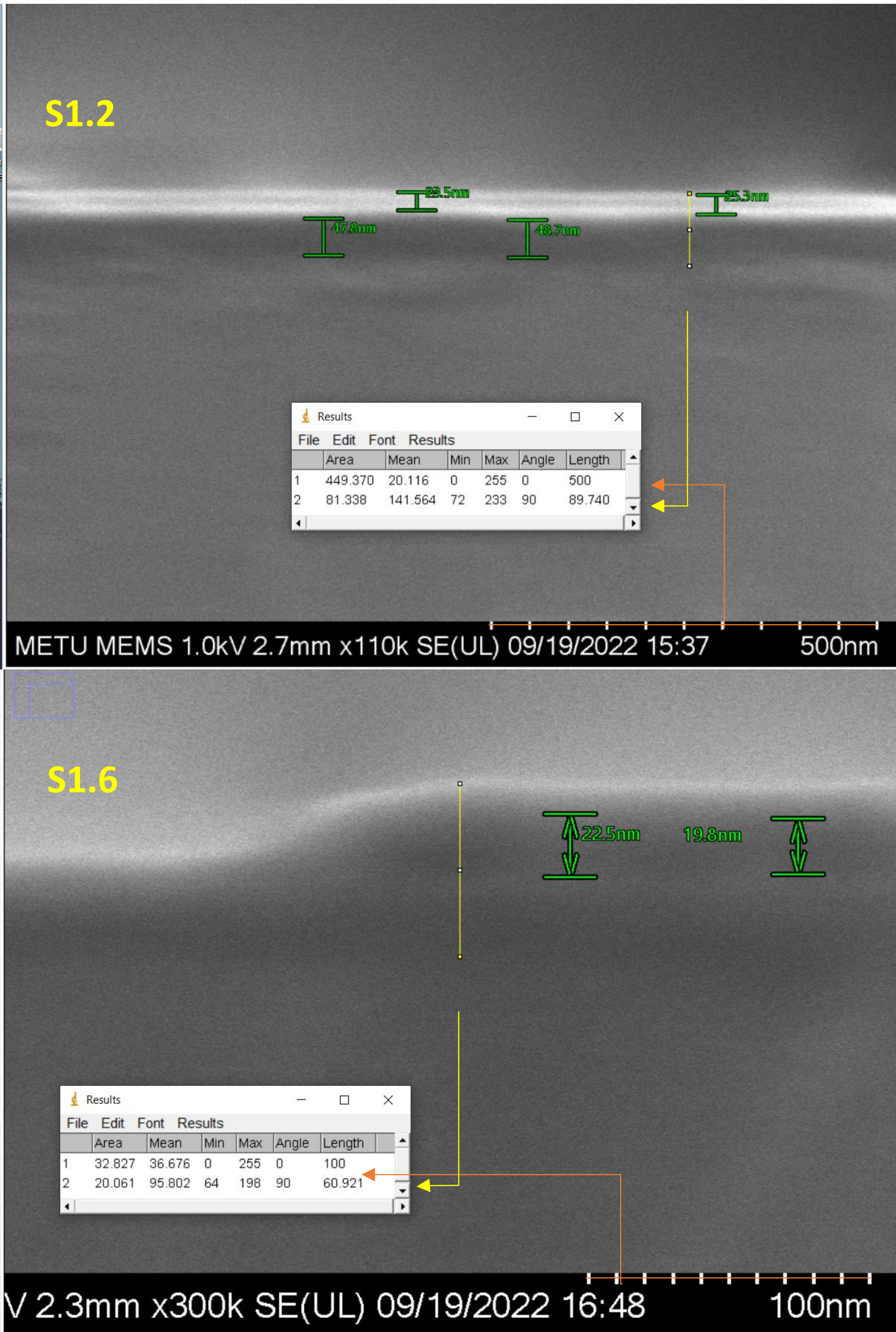

Figure 39 - Cross sectional measurement of the S1.2 and S1.6 samples

3.5 Effect of Annealing on the THz Transmission

Thin films with lower metal content SQ1 samples are exposed to an annealing step to examine annealing effects on the thin films. As can be seen in the Figure 40, transmitted THz signals are decreased for all samples after the annealing. This is not an expected result. We should note that this samples are fabricated by using wet metal etchant for patter transfer. Since, etching mechanism of the etchant solution is considered as isotropic, there are undercuts below the PR coated parts of the structure. Isotropic etch from the sidewalls of the metal islands might be diffused during annealing step and caused some degree of thinning in the overall metal layer thickness. However, the structure is lost and thus may reduce the transmission of the THz light with the increased overall dielectrics of the films due to both an increase in the effective n of the films and the k.

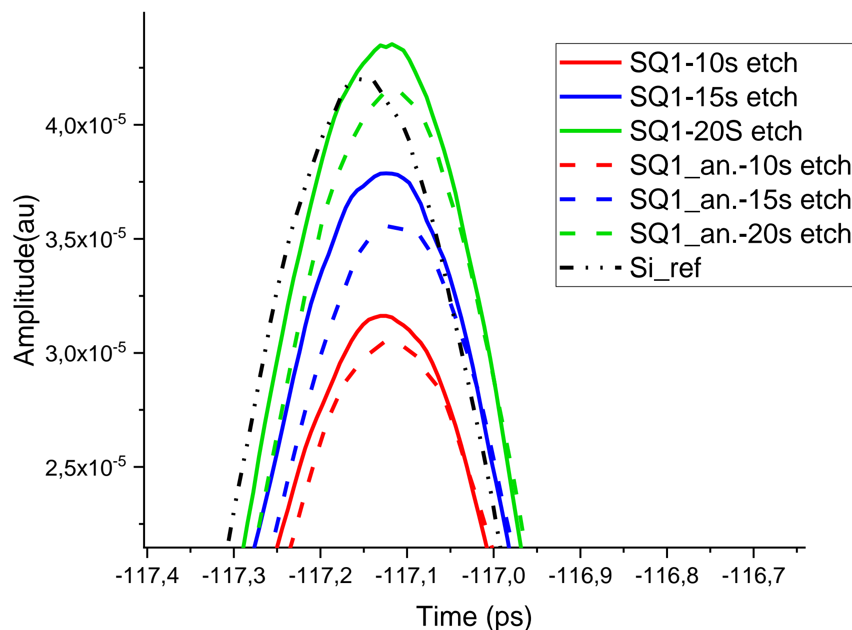

Figure 40 - Time Domain Data of the samples before and after annealing for 1 hour at 400 °C

3.6 Calculated Refractive Index of the P-Type Silicon

In here, calculated refractive index values are indicated. Using time domain data, equal numbers of data points converted into frequency domain by using Fast Fourier Transformation (FFT). Parameters of the conversion can be seen in the

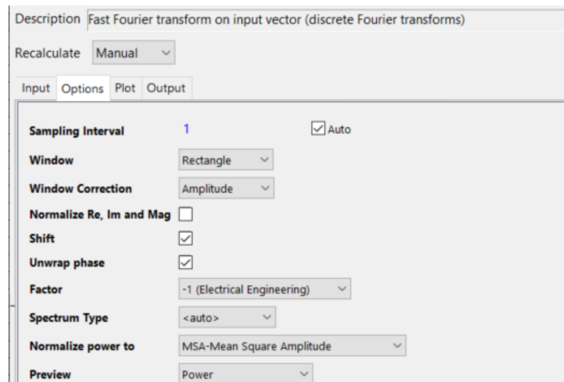

Figure 41 - FFT parameters that used in the Origin Pro Software

Figure 41.

First, frequency dependent refractive index of a p-type Si wafer was calculated by using phase difference values retrieved from the result of the FFT analysis. Time domain data used for the refractive index calculation of the P-type Silicon can be seen in Figure 42.

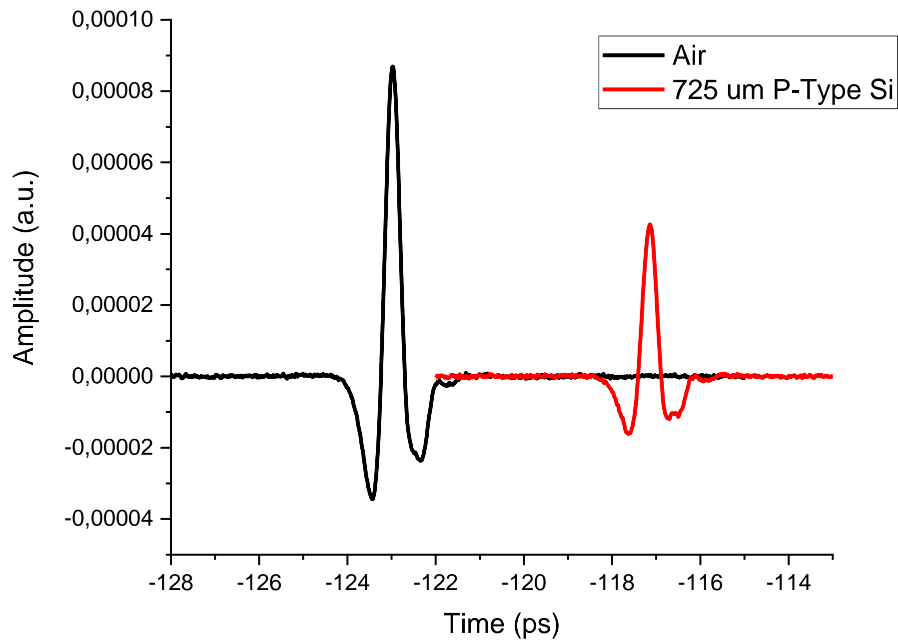

Figure 42 - THz-TDS Spectrum of the P-Type Si with respect to air

$$n = 1 + \frac{\Delta Phase * c}{2 * \pi * frequecny * 1E12 * 725E - 6}$$

Equation 4 - Equation that was used to calculate the real index, n of the P-type Si

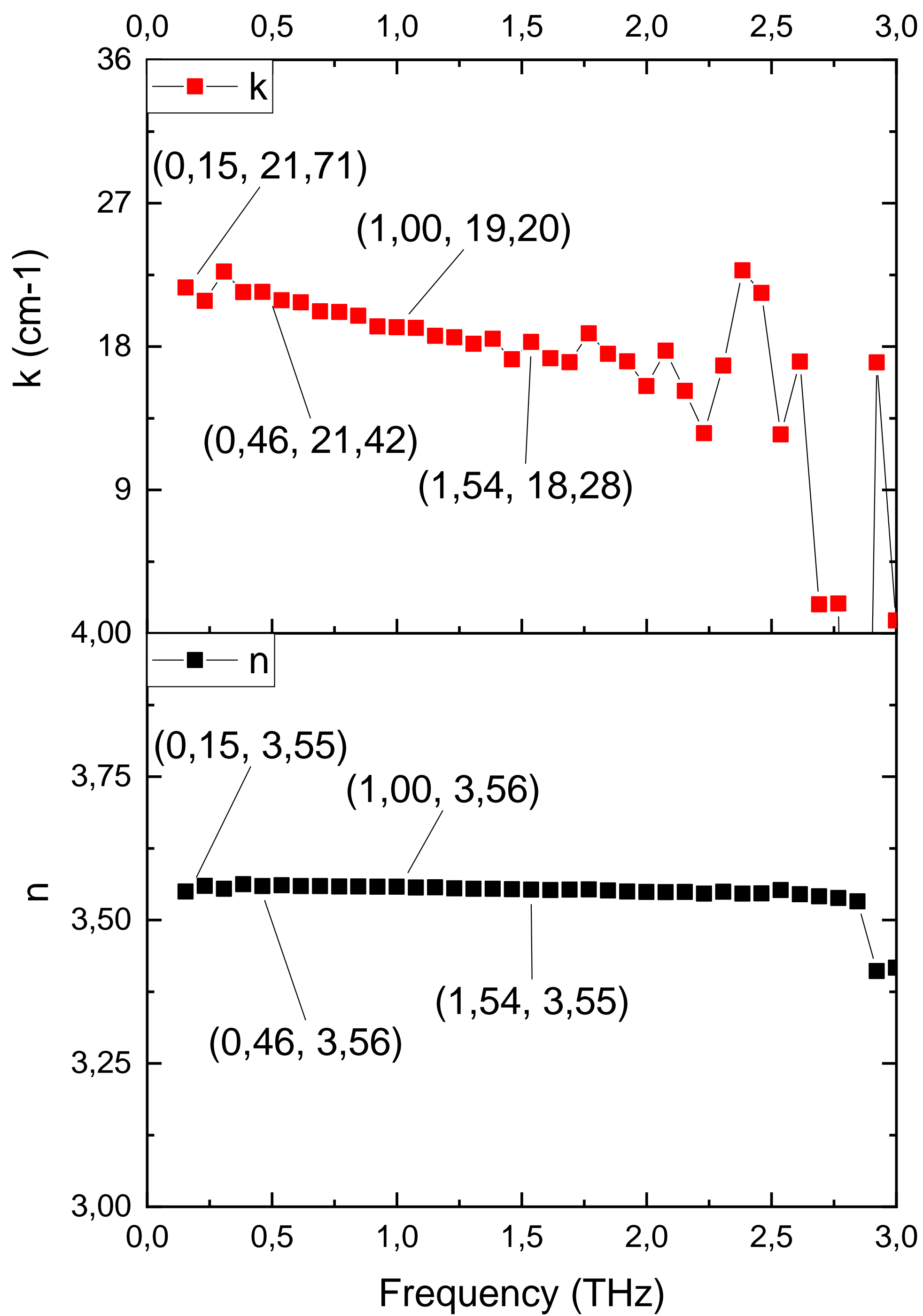

Figure 43 - Calculated n and k values of P-type Silicon

As can be seen in Figure 43, our calculated refractive index for P-type Si is 3.56 at 1 THz. At the below table, our results and the reported studies from the literature are compared.

	Our Study	Study 1 [55]	Study 2[56]
Material	Silicon	Silicon	Silicon
Dopant	Boron	Boron	Boron
Type	P	P	P
Orientation	<100>	-	<100>
Wafer thickness (μm)	725	225	525
Resistivity (Ω.cm)	5(min) - 30(max)	30	0.010–0.020
Reported n at 1 THz	3.56	3.4 (avg of 10 measurement)	4.5

3.7 Simulated vs Measured Data

In addition to the measurements, the response of micropatterned metal dielectric composite thin films fabricated on P-type Si substrates was simulated by Prof. Dr. Hakan Altan using the CST Microwave Studio Frequency Domain Solver in the 0.1 – 1 THz frequency region. The P-type Si substrate data optimization was achieved by calculating the available P-type substrate's refractive index. In addition, a multilayer film structure was modeled on a p-type silicon substrate with a patterned metal layer within dielectric silicon nitride layers and simulated in terms of percent transmittance in the sub-1-THz region. Modeled structures were produced at METU MEMS Center and measured with THz-TDS to compare the measured data with the simulated model results. As seen in Figure 44, the volumetric filling factor difference of the samples does not cause a significant difference in terms of power transmittance. The simulation results obtained are shown in Figure 45. Both simulation and measurement results have an increase in power transmission with

frequency increase. This trend is matched in all examples. Although the spectral behaviors are similar, frequency dependent transmission shows that both SQ2 (green) and circle (blue) have lower transmission than SQ1 (red), like the experimental data.

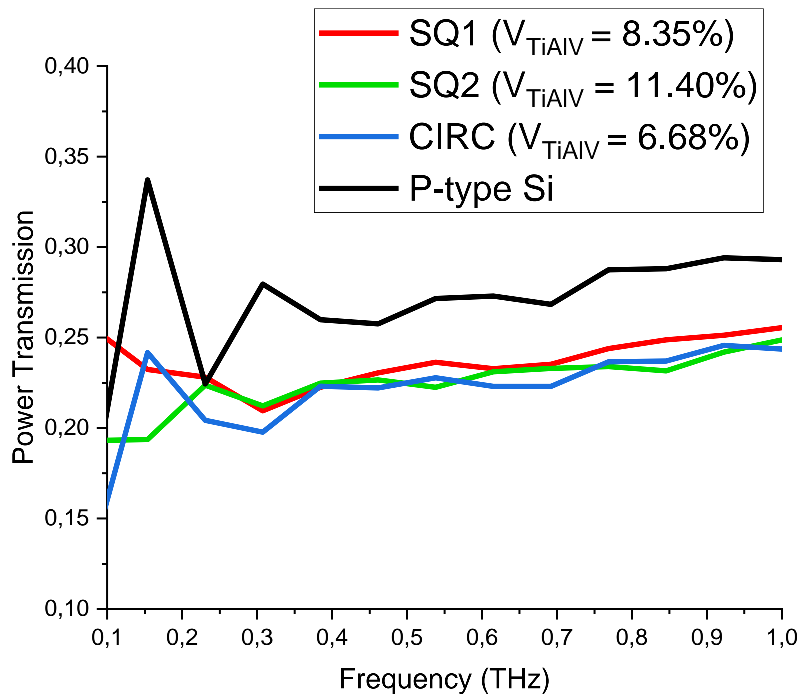

Figure 44 - Frequency Domain Power Transmission Data with respect to Air (SQ1, SQ2, and CIRC)

In order to simulate the response of the tailored micro-patterned metal dielectric composite thin films fabricated on p-type Si substrates, CST Microwave Studio Frequency Domain Solver in the 0.1 – 1 THz frequency region is implemented. The 2 x 2μm size unit cells with varying metal patterned geometry (SQ1 – 1.2 x 1.2μm, SQ2 - 1.4 x 1.4μm, and CIRC – R = 1.2μm as aforementioned) that make up the micro-patterned films are shown in Figure 46.

In addition, the Bruggeman effect medium approach was used to calculate the dielectric parameters of the composite medium, using a fill factor of 1/3 and assuming the conductivity of the metal additive to be that of Au. These results were used to simulate the interaction of this film with THz waves, the thickness of which was kept the same as the above micropatterned thin films. The transmission results obtained in this way are shown below.

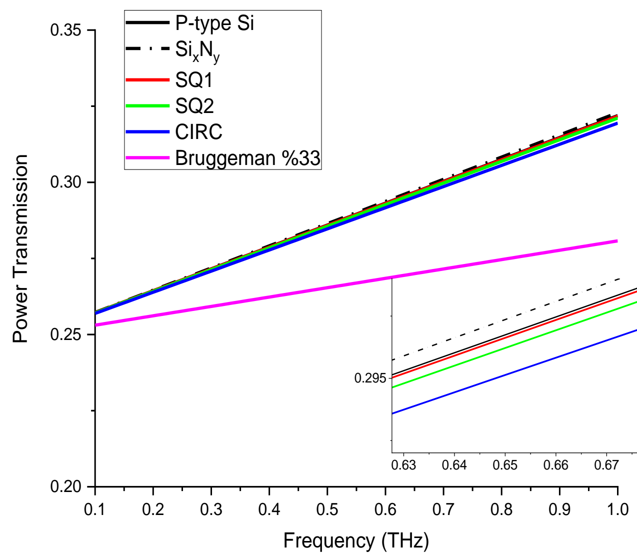

Figure 45 - CST Microwave Simulations of the thin-films (Completed by Prof. Dr. Hakan Altan)

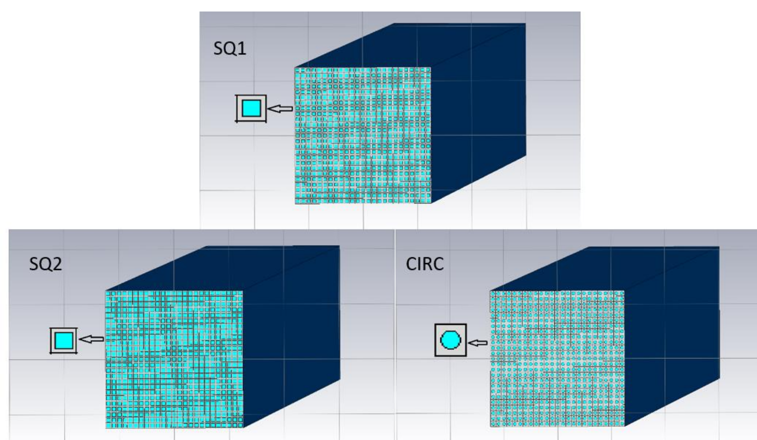

Figure 46 - Simulated effective mediums

CHAPTER 4

CONCLUSION

In this study, THz responses of the effective mediums (sub wavelength sized, composite) with TiAlV metal inserted in Si_xN_y dielectric media were investigated with the aim of potential applications in uncooled THz microbolometers. Fabrication of the thin-films were completed successfully. The relationship between optical response in sub-1 THz region and the fabrication parameters such as the etching method, etching time, amount of volumetric metal content and the addition of an annealing step, is investigated. Morever, result of a simulation model that uses Bruggeman effective medium theory (EMT) and the fabricated films are compared with each other. After completion of the optimization of process flow, the optical effect of the wet etching and its duration was investigated. Although the overall behaviors are very similar, the measured power transmission appears to be lower than the simulated power transmission for all samples. This may be due to differences in the patterned structures of simulated and experimental samples. While the simulation accepts an ideal structure, it is expected that the experimental structure will not be uniform shapes and as good as the model.. Increasing volumetric metal content of the thin-films (S1.2, S1.4, S1.5, and S1.6) has shown higher transmission levels than SQ1, SQ2, and CIRC samples. This can be explained with the decreased surface roughness of the second batch of the fabrication (S1.X samples). By using mask reversal and SixNy etching, non-uniformities of the films are minimized. That can decreases scattering effects due to defects on the surface. However, there was no relationship between surface area of the embedded metal parts and THz transmission of the samples for the sub-1 THz region. S1.6 and S1.2 samples have shown similar transmission levels altough their volumetric metal content is significantly different. Further investigation has shown that because of the non-uniformity of the PVD Sputtering method on the 8”

wafer, total thicknesses of the metal layer of the samples show slight differences. For the samples of S1.2, S1.4 and S1.5 are The dielectric Si_xN_y layers and the TiAlV layer could not be seen clearly in the cross-sectional SEM investigation but, total thicknesses of the films show slight differences which results with higher transmission than anticipated. Further studies are needed for the optimization of the fabrication. Finally, THz response of the fabricated thin films with periodic metals in the scale of the sub-wavelength and the simulations based on Bruggeman EMT are in agreement with each other.

REFERENCES

[1] G. Valušis, A. Lisauskas, H. Yuan, W. Knap, and H. G. Roskos, "Roadmap of terahertz imaging 2021," *Sensors*, vol. 21, no. 12. MDPI AG, Jun. 02, 2021. doi: 10.3390/s21124092.

[2] R. A. Lewis, "A review of terahertz detectors," *J Phys D Appl Phys*, vol. 52, no. 43, 2019, doi: 10.1088/1361-6463/ab31d5.

[3] H. Chen, H. Sarieddeen, T. Ballal, H. Wymeersch, M.-S. Alouini, and T. Y. Al-Naffouri, "A Tutorial on Terahertz-Band Localization for 6G Communication Systems," Oct. 2021, doi: 10.1109/comst.2022.3178209.

[4] S. F. Busch, M. Weidenbach, M. Fey, F. Schäfer, T. Probst, and M. Koch, "Optical Properties of 3D Printable Plastics in the THz Regime and their Application for 3D Printed THz Optics," *J Infrared Millim Terahertz Waves*, vol. 35, no. 12, pp. 993–997, 2014, doi: 10.1007/s10762-014-0113-9.

[5] F. Friederich *et al.*, "THz active imaging systems with real-time capabilities," *IEEE Trans Terahertz Sci Technol*, vol. 1, no. 1, pp. 183–200, 2011, doi: 10.1109/TTHZ.2011.2159559.

[6] J. F. Federici *et al.*, "THz imaging and sensing for security applications - Explosives, weapons and drugs," *Semicond Sci Technol*, vol. 20, no. 7, 2005, doi: 10.1088/0268-1242/20/7/018.

[7] S. Gui, J. Li, and Y. Pi, "Security Imaging for Multi-Target Screening Based on Adaptive Scene Segmentation with Terahertz Radar," *IEEE Sens J*, vol. 19, no. 7, pp. 2675–2684, 2019, doi: 10.1109/JSEN.2018.2889884.

[8] D. Čibiraitė-Lukenskienė, K. Ikamas, T. Lisauskas, V. Krozer, H. G. Roskos, and A. Lisauskas, "Passive detection and imaging of human body radiation using an uncooled field-effect transistor-based THZ detector,"

Sensors (Switzerland), vol. 20, no. 15, pp. 1–14, 2020, doi: 10.3390/s20154087.

[9] Y. S. Aytekin, M. Köktürk, A. Zaczek, T. M. Korter, E. J. Heilweil, and O. Esenturk, “Optical properties of Meloxicam in the far-infrared spectral region,” *Chem Phys*, vol. 512, no. 312, pp. 36–43, 2018, doi: 10.1016/j.chemphys.2018.04.022.

[10] Y. S. Aytekin, M. Kokturk, A. Zaczek, T. M. Korter, E. J. Heilwei, and O. Esenturk, “Optical Properties of Active Pharmaceutical Ingredients in Terahertz Region,” *International Conference on Infrared, Millimeter, and Terahertz Waves, IRMMW-THz*, vol. 2019-Septe, pp. 4–5, 2019, doi: 10.1109/IRMMW-THz.2019.8874394.

[11] P. Zolliker, M. Shalaby, E. Söllinger, E. Mavrona, and E. Hack, “Real-time high resolution thz imaging with a fiber-coupled photo conductive antenna and an uncooled microbolometer camera,” *Sensors*, vol. 21, no. 11, 2021, doi: 10.3390/s21113757.

[12] Y. H. Tao, A. J. Fitzgerald, and V. P. Wallace, “Non-contact, non-destructive testing in various industrial sectors with terahertz technology,” *Sensors (Switzerland)*, vol. 20, no. 3, 2020, doi: 10.3390/s20030712.

[13] N. Rajic and N. Street, “A performance comparison between cooled and uncooled infrared detectors for thermoelastic stress analysis,” *Quant Infrared Thermogr J*, vol. 11, no. 2, pp. 207–221, 2014, doi: 10.1080/17686733.2014.962835.

[14] I. Ryger *et al.*, “Uncooled Antenna-Coupled Microbolometer for Detection of Terahertz Radiation,” *J Infrared Millim Terahertz Waves*, vol. 42, no. 4, pp. 462–478, Apr. 2021, doi: 10.1007/s10762-021-00781-y.

[15] R. T. Rajendra Kumar *et al.*, “Pulsed laser deposited vanadium oxide thin films for uncooled infrared detectors,” *Sens Actuators A Phys*, vol. 107, no. 1, pp. 62–67, 2003, doi: 10.1016/S0924-4247(03)00233-4.

[16] N. Oda *et al.*, "Microbolometer Terahertz Focal Plane Array and Camera with Improved Sensitivity in the Sub-Terahertz Region," *J Infrared Millim Terahertz Waves*, vol. 36, no. 10, pp. 947–960, 2015, doi: 10.1007/s10762-015-0184-2.

[17] A. Banerjee, H. Satoh, D. Elamaran, Y. Sharma, N. Hiromoto, and H. Inokawa, "Performance improvement of on-chip integrable terahertz microbolometer arrays using nanoscale meander titanium thermistor," *J Appl Phys*, vol. 125, no. 21, 2019, doi: 10.1063/1.5083643.

[18] H. Cui, J. Yao, and C. Wan, "The study on THz wave propagation feature in atmosphere," *J Phys Conf Ser*, vol. 276, no. 1, 2011, doi: 10.1088/1742-6596/276/1/012225.

[19] Y. Tanrıkulu, "an Uncooled Infrared Microbolometer Detector Array Using Surface Micromachined Mems Technology a Thesis Submitted To the Graduate School of Natural and Applied Sciences of Middle East Technical University By in Partial Fulfilment of the Requirements for T," no. August, 2007.

[20] N. Nemoto *et al.*, "High-Sensitivity and Broadband, Real-Time Terahertz Camera Incorporating a Micro-Bolometer Array with Resonant Cavity Structure," *IEEE Trans Terahertz Sci Technol*, vol. 6, no. 2, pp. 175–182, 2016, doi: 10.1109/TTHZ.2015.2508010.

[21] N. Oda, I. Hosako, T. Ishi, H. Minamide, C. Otani, and N. Sekine, "The need of terahertz cameras for standardizing sensitivity measurements," *J Infrared Millim Terahertz Waves*, vol. 35, no. 8, pp. 671–685, 2014, doi: 10.1007/s10762-014-0073-0.

[22] J. Gou, Q. Niu, K. Liang, J. Wang, and Y. Jiang, "Frequency Modulation and Absorption Improvement of THz Micro-bolometer with Micro-bridge Structure by Spiral-Type Antennas," *Nanoscale Res Lett*, vol. 13, 2018, doi: 10.1186/s11671-018-2484-7.

[23] I. Escorcia, D. R. S. Cumming, J. P. Grant, and L. Gouveia, "Terahertz imagers based on metamaterial structures monolithically integrated in standard CMOS technologies," vol. 1065617, no. May 2018, p. 39, 2018, doi: 10.1117/12.2304335.

[24] F. Alves, L. Pimental, D. Grbovic, and G. Karunasiri, "MEMS terahertz-to-infrared band converter using frequency selective planar metamaterial," *Sci Rep*, vol. 8, no. 1, pp. 1–14, 2018, doi: 10.1038/s41598-018-30858-z.

[25] H. Bilgin, A. D. Yalcinkaya, and H. Torun, "MEMS-based terahertz detectors," *Procedia Eng*, vol. 120, pp. 15–19, 2015, doi: 10.1016/j.proeng.2015.08.556.

[26] D. X. Zhou, E. P. J. Parrott, D. J. Paul, and J. A. Zeitler, "Determination of complex refractive index of thin metal films from terahertz time-domain spectroscopy," *J Appl Phys*, vol. 104, no. 5, 2008, doi: 10.1063/1.2970161.

[27] Naval Air Warfare Center Weapons Division, *Electronic Warfare and Radar Systems Engineering Handbook 2013 NAWCWD TP 8347 Fourth Edition*. 2013.

[28] Y. J. Jen, W. C. Liu, T. K. Chen, S. W. Lin, and Y. C. Jhang, "Design and deposition of a metallike and admittance-matching metamaterial as an ultra-thin perfect absorber," *Sci Rep*, vol. 7, no. 1, pp. 1–10, 2017, doi: 10.1038/s41598-017-03392-7.

[29] "BATOP.de-devices-PCA." Accessed: Jun. 07, 2022. [Online]. Available: https://www.batop.de/information/PCA_infos.html

[30] S. Mondal, N. Flora Boby Edwin, and V. Rathinasamy, "Interdigitated Photoconductive Antenna for Efficient Terahertz Generation and Detection." [Online]. Available: www.intechopen.com

[31] N. M. Burford and M. O. El-Shenawee, "Review of terahertz photoconductive antenna technology," *Optical Engineering*, vol. 56, no. 1, p. 010901, Jan. 2017, doi: 10.1117/1.oe.56.1.010901.

[32] D. R. Bacon, J. Madéo, and K. M. Dani, "Photoconductive emitters for pulsed terahertz generation," *Journal of Optics (United Kingdom)*, vol. 23, no. 6, Jun. 2021, doi: 10.1088/2040-8986/abf6ba.

[33] Y.-S. Lee, *Principles of terahertz science and technology*. Springer, 2009.

[34] G. Gallot and D. Grischkowsky, "Electro-optic detection of terahertz radiation," 1999.

[35] P. C. M. Planken, C. E. W. M. van Rijmenam, and R. N. Schouten, "Opto-electronic pulsed THz systems," *Semiconductor Science and Technology*, vol. 20, no. 7. Jul. 01, 2005. doi: 10.1088/0268-1242/20/7/001.

[36] T. Ao *et al.*, "Terahertz Metamaterial-Based Microbolometers Fabricated by Conventional MEMS," *Optics and Photonics Journal*, vol. 06, no. 08, pp. 215–218, 2016, doi: 10.4236/opj.2016.68b036.

[37] Y. Liu and X. Zhang, "Metamaterials: A new frontier of science and technology," *Chem Soc Rev*, vol. 40, no. 5, pp. 2494–2507, 2011, doi: 10.1039/c0cs00184h.

[38] A. Lanzi, "Hybrid Terahertz Metamaterials: From Perfect Absorption to Superconducting Plasmonics," *UC San Diego Electronic Theses and Dissertations*, p. 214, 2018.

[39] D. R. Smith, J. B. Pendry, and M. C. K. Wiltshire, "Metamaterials and negative refractive index," *Science (1979)*, vol. 305, no. 5685, pp. 788–792, 2004, doi: 10.1126/science.1096796.

[40] P. Wang, M. E. Nasir, A. v. Krasavin, W. Dickson, Y. Jiang, and A. v. Zayats, "Plasmonic Metamaterials for Nanochemistry and Sensing," *Acc*

Chem Res, vol. 52, no. 11, pp. 3018–3028, 2019, doi: 10.1021/acs.accounts.9b00325.

[41] C. M. Watts, "Metamaterials and their applications towards novel imaging technologies," *ProQuest Dissertations and Theses*, p. 103, 2015, [Online]. Available: http://login.ezproxy.library.ualberta.ca/login?url=http://search.proquest.com/docview/1719268970?accountid=14474%5Cnhttp://resolver.library.ualberta.ca/resolver?url_ver=Z39.88-2004&rft_val_fmt=info:ofi/fmt:kev:mtx:dissertation&genre=dissertations+%26+thes

[42] N. I. Landy, S. Sajuyigbe, J. J. Mock, D. R. Smith, and W. J. Padilla, "Perfect metamaterial absorber," *Phys Rev Lett*, vol. 100, no. 20, pp. 1–4, 2008, doi: 10.1103/PhysRevLett.100.207402.

[43] H. T. Chen, W. J. Padilla, J. M. O. Zide, A. C. Gossard, A. J. Taylor, and R. D. Averitt, "Active terahertz metamaterial devices," *Nature*, vol. 444, no. 7119, pp. 597–600, 2006, doi: 10.1038/nature05343.

[44] Y. Chang, J. Wei, and C. Lee, "Metamaterials - From fundamentals and MEMS tuning mechanisms to applications," *Nanophotonics*, vol. 9, no. 10, pp. 3049–3070, 2020, doi: 10.1515/nanoph-2020-0045.

[45] A. Andryieuski and A. v. Lavrinenko, "Graphene metamaterials based tunable terahertz absorber: effective surface conductivity approach," *Opt Express*, vol. 21, no. 7, p. 9144, 2013, doi: 10.1364/oe.21.009144.

[46] S. J. Park, S. A. N. Yoon, and Y. H. Ahn, "Dielectric constant measurements of thin films and liquids using terahertz metamaterials," *RSC Adv*, vol. 6, no. 73, pp. 69381–69386, 2016, doi: 10.1039/c6ra11777e.

[47] W. J. Padilla, "Metamaterial devices for the terahertz gap," *APMC 2009 - Asia Pacific Microwave Conference 2009*, pp. 1297–1298, 2009, doi: 10.1109/APMC.2009.5384460.

[48] S. J. Park, S. A. N. Yoon, and Y. H. Ahn, “Supplementary Information for Dielectric constant measurements of thin films and liquids using terahertz metamaterials,” 2016.

[49] Y. Du, W. Wei, X. Zhang, and Y. Li, “Tuning Metamaterials Nanostructure of Janus Gold Nanoparticle Film for Surface-Enhanced Raman Scattering,” *Journal of Physical Chemistry C*, vol. 122, no. 14, pp. 7997–8002, 2018, doi: 10.1021/acs.jpcc.8b00676.

[50] C. Vinodbabu, G. T. Rao, N. B. Reddy, and G. v. Zyryanov, “A review on magnetron sputter coatings,” in *AIP Conference Proceedings*, Nov. 2020, vol. 2280. doi: 10.1063/5.0018142.

[51] C. Grant Willson, R. R. Dammel, and A. Reiser, “Photoresist materials: a historical perspective”, doi: 10.1117/12.275921.

[52] A. Reiser *et al.*, “The molecular mechanism of novolak–diazonaphthoquinone resists”, doi: 10.1016/s0014-3057(01)00230-0.

[53] Alan J. Telecky, “Photoresist and Ion-ExchangeChemistry of HafSOx.”

[54] www.MicroChemicals.com, “Chapter 01 MicroChemicals ®-Fundamentals of Microstructuring COMPOSITION AND PROPERTIES OF AZ ® AND TI PHOTORESISTS.” [Online]. Available: www.microchemicals.com/downloads/application_notes.html

[55] L. Duvillaret, F. Garet, and J. L. Coutaz, “A reliable method for extraction of material parameters in terahertz time-domain spectroscopy,” *IEEE Journal on Selected Topics in Quantum Electronics*, vol. 2, no. 3, pp. 739–745, Sep. 1996, doi: 10.1109/2944.571775.

[56] N. Chudpooti *et al.*, “Wideband dielectric properties of silicon and glass substrates for terahertz integrated circuits and microsystems,” *Mater Res Express*, vol. 8, no. 5, May 2021, doi: 10.1088/2053-1591/abf684.